INTERNATIONAL JOURNAL FOR NUMERICAL METHODS IN FLUIDS
Int. J. Numer. Meth. Fluids **31**: 983–1017 (1999)

AN UNSTEADY INCOMPRESSIBLE NAVIER–STOKES SOLVER FOR LARGE EDDY SIMULATION OF TURBULENT FLOWS

WON-WOOK KIM AND SURESH MENON*

School of Aerospace Engineering, Georgia Institute of Technology, Atlanta, GA 30332-0150, USA

SUMMARY

An unsteady incompressible Navier–Stokes solver that uses a dual time stepping method combined with spatially high-order-accurate finite differences, is developed for large eddy simulation (LES) of turbulent flows. The present solver uses a primitive variable formulation that is based on the artificial compressibility method and various convergence–acceleration techniques are incorporated to efficiently simulate unsteady flows. A localized dynamic subgrid model, which is formulated using the subgrid kinetic energy, is employed for subgrid turbulence modeling. To evaluate the accuracy and the efficiency of the new solver, *a posteriori* tests for various turbulent flows are carried out and the resulting turbulence statistics are compared with existing experimental and direct numerical simulation (DNS) data. Copyright © 1999 John Wiley & Sons, Ltd.

KEY WORDS: unsteady incompressible Navier–Stokes; turbulent flows; large eddy simulation; dynamic subgrid model

1. INTRODUCTION

Unsteady simulations of turbulent incompressible flows are time-consuming because of the elliptic nature of the governing equations. Although unsteady incompressible flows can be simulated using compressible flow solvers by setting the Mach number very low, this approach becomes increasingly inefficient with decreasing Mach numbers because of the limitation on the permissible time step. An alternate approach is to solve the unsteady incompressible Navier–Stokes equations iteratively at each instant to enforce the incompressibility constraint. For example, in the artificial compressibility method [1] (and similarly, in the marker and cell (MAC) method [2]), each physical time step is completed by subiterations, which are necessary to obtain the pseudo-time steady state solution. Alternatively, in the fractional step method [3], the pressure Poisson equation used to project the non-solenoidal velocity onto the divergence-free space, is iteratively solved. Although much more efficient than the compressible solvers in the incompressible regime, these iterative solvers are still computationally expensive.

The computational expense of carrying out unsteady turbulent flow simulations is also due to the very large number of grid points that are required to resolve the wide range of length scales present in the flow. To accurately resolve all these length scales, higher-order difference schemes [4,5] are desirable for spatial discretization. This requirement further increases the

* Correspondence to: School of Aerospace Engineering, Georgia Institute of Technology, Atlanta, GA 30332-0150, USA. Tel.: +1 404 8949126; fax: +1 404 8942760; e-mail: menon@falcon.ae.gatech.edu

CCC 0271–2091/99/220983–35$17.50

Received 10 February 1997
Revised 6 October 1998

expense. Finally, to ensure temporal accuracy, the computational time step has to be less than the smallest turbulent time scale resolved by the computational grid [6]. All these requirements make direct numerical simulation (DNS) of unsteady turbulent flows computationally very demanding.

When DNS is not an option, a method called large eddy simulation (LES) has become a viable approach to study unsteady turbulent flows at a reduced cost. In LES, all scales larger than the grid resolution are resolved both spatially and temporally, while the effect of the scales smaller than the grid is modeled using subgrid models. The accuracy of the LES method, therefore, depends significantly on the ability of the subgrid model to characterize the effect of the unresolved motion on the resolved scales. Classically, it was assumed that the small scales are isotropic (which is true when the entire inertial range is resolved and only the dissipation scales are modeled) and a simple but universal subgrid model for general application was sought. The classical algebraic eddy viscosity model by Smagorinsky [7] is a good example. However, results showed that the algebraic model is accurate only as long as the full inertial range is resolved, and even then the 'constant' of the model had to be tuned for different flows making the original idea of a universally applicable model questionable. The recent development of the dynamic approach originally proposed by Germano *et al*. [8] whereby the 'constant' of the algebraic model is computed as a part of the solution itself resulted in a major advancement in subgrid modeling. Although studies have shown the superior ability of this dynamic model, there remains some inherent limitations of this approach that have not yet been fully resolved. These limitations have been discussed by many researchers [8–11]. In any event due to the nature of the algebraic model (discussed later), very high resolution is required for accurate simulations. This significantly limits the ability to conduct LES of high-Reynolds number flows since the resource requirements (computer time and memory) quickly exceed availability.

In this study, the capability of an incompressible solver which is computationally efficient and accurate for unsteady turbulent flow simulations is discussed. The algorithm is based on a pseudo-compressibility, dual-time stepping scheme [12,13]. Although this methodology has been around for quite some time, the ability of this scheme for direct and large eddy simulations has not yet been studied in detail. The present study addresses these issues by carrying out a systematic study of the capability of this algorithm. Since LES of engineering flows (i.e. in complex domains) is of eventual interest, the accuracy of the high-order physical space finite differencing scheme (used in this algorithm) is carefully addressed. In an earlier DNS study [14] using this solver, the Kolmogorov-scaled energy and dissipation spectra of decaying isotropic turbulence using the present physical space solver were compared with the results obtained using a well-established pseudo-spectral code by Rogallo [15]. Very good agreement over nearly the entire wavenumber space was obtained. Detailed comparisons of the various statistical quantities (such as the dissipation rate, skewness, etc.) also showed that the present solver is capable of reproducing statistics very similar to those obtained by the spectral code. This earlier study established the basic capability of the DNS version of this solver.

The present paper discusses the ability of the present solver for carrying out LES, especially in high-Reynolds number flows. Since accurate LES implies accurate modeling of the subgrid-scale effects (especially in high-Reynolds number flows) as a part of the numerical approach, the present paper also discusses the capability of a localized dynamic subgrid model [11,16] that has demonstrated an ability to address some of the limitations of the aforementioned dynamic closure. In particular, the accuracy of the present LES approach in high-Reynolds number flows when employing reasonable grid resolution (i.e. relatively coarse when compared with the requirement for the algebraic model), is addressed.

The present dynamic model solves a transport equation for the subgrid kinetic energy [14,17] and determines the model coefficients using a localized dynamic procedure. This localized dynamic kinetic energy model is denoted LDKM for subsequent discussions (a further description of this model is given in Section 2.2 for completeness). The key advantage of this one-equation model is that it does not require the equilibrium assumption (i.e. production equals dissipation) in the small scales (which was required for the algebraic eddy viscosity subgrid model, e.g. the Smagorinsky model [7]). As a result, this model allows non-negligible kinetic energy to remain unresolved in the small scales. This ability is particularly important since it implies that in high-Reynolds number flows, a relatively coarser grid (when compared with the algebraic model LES) can be used. As demonstrated earlier [18] and in this paper, this ability is crucial for the development of LES for practical applications.

As in other dynamic models [8], two different filter levels are introduced to dynamically determine the model coefficients. However, in the LDKM, the similarity between the subgrid-scale stress tensor and the test-scale Leonard stress tensor is used to evaluate the model coefficient while in the classical dynamic models (e.g. Germano *et al.*'s dynamic mode [8]), a mathematical identity (Germano's identity) is used to implicitly model the test-scale Leonard stress tensor in terms of the difference between the model representations at two different filter levels. The scale similarity invoked in the LDKM is based on experimental observation by Liu *et al.* [19] in high-Reynolds number turbulent jets. This feature allows the LDKM to overcome some of the inherent shortcomings of the earlier dynamic models. For instance. unlike the Germano-type dynamic models, no mathematical inconsistency [9] occurs in the method and no *ad hoc* procedures are required. The numerical instability caused by the ill-conditioning problem [8] and the prolonged presence of a negative model coefficient [10] has been prevented in the LDKM by the present dynamic approach. Some details of this dynamic procedure are given below.

This paper is organized as follows. The governing equations and the dynamic subgrid model is described in the next section. In Section 3, the numerical method and its accuracy and capability is described. In Section 4, *a posteriori* test results from various benchmark turbulent flow problems are presented and discussed and conclusions are summarized in Section 5.

2. GOVERNING EQUATIONS

In this section, we briefly summarize the LES equations and the dynamic subgrid model developed for this study.

2.1. Filtered Navier–Stokes equations

In LES, all the flow variables are decomposed into a resolved large-scale component (denoted by an overbar) and an unresolved subgrid-scale (SGS) component by applying a filtering operation

$$\bar{f}(x_i) = \int f(x_i')G(x_i, x_i')\,\mathrm{d}x_i', \tag{1}$$

where f represents an arbitrary flow variable, x_i denotes the spatial co-ordinates, G is the filter function and the integral is over the entire domain. Applying the filtering operation (in the present study, a low-pass filter of the computational mesh which is consistent with finite volume methods (FVM) [17] is used, hence the characteristic size of this filter is the grid width

$\bar{\Delta}$), the following incompressible Navier–Stokes equations for the resolved motion are obtained:

$$\frac{\partial \bar{u}_i}{\partial x_i} = 0, \tag{2}$$

$$\frac{\partial \bar{u}_i}{\partial t} + \bar{u}_j \frac{\partial \bar{u}_i}{\partial x_j} = -\frac{\partial}{\partial x_j}\left(\frac{\bar{p}}{\rho}\delta_{ij} + \tau_{ij}\right) + \nu \frac{\partial^2 \bar{u}_i}{\partial x_j \partial x_j}, \tag{3}$$

where $\bar{u}_i(x_i, t)$ is the resolved velocity field, t denotes the physical time, $\bar{p}$ is the resolved pressure, ρ is the mass density, δ_{ij} is the Kronecker delta, and ν is the kinematic viscosity. Hereafter, the constant ρ will be absorbed into the pressure and, therefore, it will be dropped from the subsequent equations. The effect of the unresolved small scales appear as the subgrid scale (SGS) stress tensor

$$\tau_{ij} = \overline{u_i u_j} - \bar{u}_i \bar{u}_j \tag{4}$$

in the LES equations and must be modeled. In the present study, this term is parameterized using the subgrid model described in the following section.

2.2. Localized dynamic subgrid model

Two parameters, a length scale and a velocity scale, need to be defined to develop a subgrid model. Here, the grid scale is used to characterize the length scale and the velocity scale is obtained by determining the SGS kinetic energy

$$k_{\mathrm{SGS}} = \frac{1}{2}(\overline{u_k u_k} - \bar{u}_k \bar{u}_k), \tag{5}$$

using the following transport equation [14,17]:

$$\frac{\partial k_{\mathrm{SGS}}}{\partial t} + \bar{u}_i \frac{\partial k_{\mathrm{SGS}}}{\partial x_i} = -\tau_{ij}\frac{\partial \bar{u}_i}{\partial x_j} - \varepsilon_{\mathrm{SGS}} + \frac{\partial}{\partial x_i}\left(\nu_T \frac{\partial k_{\mathrm{SGS}}}{\partial x_i}\right). \tag{6}$$

Here, the three terms on the right-hand side represent respectively the production, the dissipation and the diffusion of k_{SGS}. Also, ν_T denotes the eddy viscosity (defined below). Using k_{SGS}, the SGS stress tensor τ_{ij} is modeled as [17,20]

$$\tau_{ij} = -2C_\tau \bar{\Delta} k_{\mathrm{SGS}}^{1/2} \bar{S}_{ij} + \frac{2}{3}\delta_{ij} k_{\mathrm{SGS}}, \tag{7}$$

where C_τ is an adjustable coefficient to be determined dynamically, $\bar{\Delta}$ is the grid size and $\bar{S}_{ij}$ is the resolved-scale strain rate tensor

$$\bar{S}_{ij} = \frac{1}{2}\left(\frac{\partial \bar{u}_i}{\partial x_j} + \frac{\partial \bar{u}_j}{\partial x_i}\right). \tag{8}$$

Implicit in Equation (7) is the parameterization of the eddy viscosity ν_T by using $\bar{\Delta}$ as the characteristic length scale and k_{SGS} as the characteristic velocity scale. Thus,

$$\nu_T = C_\tau \bar{\Delta} k_{\mathrm{SGS}}^{1/2}. \tag{9}$$

Equation (6) is closed once the SGS dissipation rate $\varepsilon_{\mathrm{SGS}}$ is modeled. Using simple scaling arguments, $\varepsilon_{\mathrm{SGS}}$ is usually modeled as [17,20]

$$\varepsilon_{\mathrm{SGS}} = C_\varepsilon \frac{k_{\mathrm{SGS}}^{3/2}}{\bar{\Delta}}, \tag{10}$$

where C_ε is another coefficient also to be determined dynamically.

The dynamic procedure to evaluate C_τ and C_ε requires using a test filter field that is constructed from the grid-scale field by applying a test filter characterized by $\hat{\Delta}$ (typically [8] $\hat{\Delta} = 2\bar{\Delta}$). A test filter shape that is consistent with the grid filter in form is usually preferred [8]. Some researchers [21,22] have investigated the effect of various filter shapes on the turbulence statistics. However, the optimal choice (in terms of accuracy and efficiency) of filters for a particular numerical method has not yet been established. In the present study, the top-hat filter based on the trapezoidal rule is employed for the test filter (and is implicit in the grid filter as noted by Schumann [17]). If the application of the test filter on any variable, ϕ, is denoted by $\hat{\phi}$, the test-scale Leonard stress tensor is

$$L_{ij} = \widehat{\bar{u}_i \bar{u}_j} - \hat{\bar{u}}_i \hat{\bar{u}}_j. \tag{11}$$

Liu *et al.* [19] observed a significant similarity between τ_{ij} and L_{ij} in their experimental data obtained in the far-field of a turbulent round jet at reasonably high Reynolds number, $Re_\lambda \approx 310$ (Re_λ is the Reynolds number defined based on turbulence intensity and Taylor microscale λ). The experimental data showed that the correlation between these two stress tensors was quite high. Therefore, they suggested a SGS model based on this scale similarity: $\tau_{ij} = C_k L_{ij}$, where C_k is an adjustable constant (a value of 0.45 ± 0.15 was suggested by Liu *et al.* [19]). However, this model (which is somewhat similar, except for the test filter size, to the scale similarity model proposed earlier by Bardina *et al.* [23]) does not have sufficient dissipation and therefore cannot be used for LES. In the present study, this scale similarity assumption is employed not as a subgrid model but rather as a method to obtain the model coefficients dynamically. This key step allows the LDKM to avoid many of the earlier noted problems with the classical dynamic closure model.

At the test filter level, a resolved kinetic energy can be defined from the trace of Equation (11)

$$k_{\mathrm{test}} = \frac{1}{2}\left(\widehat{\bar{u}_k \bar{u}_k} - \hat{\bar{u}}_k \hat{\bar{u}}_k\right) \tag{12}$$

(note that $k_{\mathrm{test}} = L_{kk}/2$). This energy is similar to k_{SGS}, except that it is produced at the large scales by $-L_{ij}(\partial \hat{\bar{u}}_i / \partial x_j)$ and is dissipated by

$$e = (\nu + \nu_T)\left(\overbrace{\frac{\partial \bar{u}_i}{\partial x_j}\frac{\partial \bar{u}_i}{\partial x_j}}^{\widehat{}} - \frac{\partial \hat{\bar{u}}_i}{\partial x_j}\frac{\partial \hat{\bar{u}}_i}{\partial x_j}\right), \tag{13}$$

at the small scales. Here, $(\nu + \nu_T)$ is used since k_{test} is fully resolved at the test filter level and thus must be dissipated by both the eddy viscosity and the molecular viscosity. Since experiments suggest that τ_{ij} and L_{ij} are similar, a possible representation for L_{ij} (similar to the form used for τ_{ij} but in terms of the test-filtered variables) is

$$L_{ij} = -2C_\tau \hat{\Delta} k_{\mathrm{test}}^{1/2} \hat{\bar{S}}_{ij} + \frac{1}{3}\delta_{ij} L_{kk}. \tag{14}$$

In Equation (14) the only unknown is C_τ, whereas Equation (7) contains two unknowns τ_{ij} and C_τ. Thus, Equation (14) can be viewed as an explicit model representation for C_τ in terms of quantities resolved at the test filter level. This system of equations represents five independent equations in one unknown (i.e. overdetermined), hence the value of C_τ can be estimated only in an approximated manner by applying the least-square method suggested by Lilly [24]

$$C_\tau = \frac{1}{2}\frac{L_{ij}\sigma_{ij}}{\sigma_{lm}\sigma_{lm}}, \tag{15}$$

where

$$\sigma_{ij} = -\hat{\Delta}k_{\text{test}}^{1/2}\hat{\bar{S}}_{ij}. \tag{16}$$

Note that σ_{ij} is determined completely from quantities at the test filter level.

The above formulation can be contrasted to the classical Germano-type of dynamic closure, where the mathematical identity in terms of the model representation at the two filter levels results in the denominator of Equation (15) to be ill-conditioned (i.e. to tend to zero locally [8]). As a result, some algorithmic adjustments are typically needed (e.g. spatial averaging in a homogeneous direction [8,25], etc.). The present LDKM approach avoids this problem since the denominator (16) only contains a well-defined (and non-zero) quantity.

Similarity between the dissipation rates ε_{SGS} at the grid filter level and e at the test filter level is also invoked in the LDKM to obtain the dissipation model coefficient. Thus,

$$e = C_\varepsilon \frac{k_{\text{test}}^{3/2}}{\hat{\Delta}}. \tag{17}$$

Since Equation (17) is a single equation with one unknown, C_ε can be determined easily from

$$C_\varepsilon = \frac{(\nu + \nu_T)\hat{\Delta}[\overbrace{(\partial\bar{u}_i/\partial x_j)(\partial\bar{u}_i/\partial x_j)} - (\partial\hat{\bar{u}}_i/\partial x_j)(\partial\hat{\bar{u}}_i/\partial x_j)]}{k_{\text{test}}^{3/2}}. \tag{18}$$

In summary, by assuming a similarity between τ_{ij} and L_{ij} (which appears reasonable from experimental data), the LDKM can be formulated without employing any mathematically inconsistent or *ad hoc* procedure (the mathematical inconsistency of Germano *et al.*'s dynamic formulation [8] has been pointed out earlier by Cabot and Moin [9]). There are some more positive aspects to this approach. As noted above, the denominators of Equations (15) and (18) contain resolved quantities and, therefore, the ill-conditioning problem (seen in Germano *et al.*'s dynamic formulation [8]) is significantly relieved. The prolonged presence of negative model coefficient discussed by Lund *et al.* [10] also can be avoided in the present model since it uses the SGS kinetic energy (which is never negative). Moreover, the dynamically determined C_ε from Equation (18) does not vanish in the limit of high Reynolds number (a phenomenon that was observed in an earlier dynamic kinetic energy model formulation by Wong [26]) since $\nu + \nu_T \geq \nu$.

Analysis of results have shown that the LDKM is Galilean-invariant and satisfies well [27] the realizability conditions given by Schumann [28]. From a computational standpoint, the cost of the present dynamic procedure is not significant (about the same as that for the dynamic model by Germano *et al.* [8]) due to its simplicity. The additional computational cost is primarily due to the inclusion of a transport equation for k_{SGS}. The justification for this extra computational cost is that this approach has the aforementioned advantage over algebraic models since the equilibrium assumption is not required. Furthermore, k_{SGS} provides a more accurate estimate for the SGS velocity scale.

The results reported in this paper will demonstrate the ability of the LDKM approach when applied to high-Reynolds number flows using relatively coarse grids. Interestingly, the superior ability of the LDKM model in coarse grid LES was also recently demonstrated independently by Fureby *et al.* [27] in their comparative study of various SGS models.

2.3. Transformation of governing eqations

Following conventional methods [29], the Cartesian space (x, y, z) is mapped onto a generalized curvilinear space (ξ, η, ζ) and the governing equations, (2) and (3), are rewritten as

$$\frac{\partial}{\partial \xi}\left(\frac{U}{J}\right)+\frac{\partial}{\partial \eta}\left(\frac{V}{J}\right)+\frac{\partial}{\partial \zeta}\left(\frac{W}{J}\right)=0, \tag{19}$$

$$\frac{1}{J}\frac{\partial q}{\partial t}+\left(\frac{U}{J}\right)\frac{\partial q}{\partial \xi}+\left(\frac{V}{J}\right)\frac{\partial q}{\partial \eta}+\left(\frac{W}{J}\right)\frac{\partial q}{\partial \zeta}=-\frac{\partial E}{\partial \xi}-\frac{\partial F}{\partial \eta}-\frac{\partial G}{\partial \zeta}, \tag{20}$$

where J is the Jacobian of the transformation, and U, V and W are respectively the contravariant velocities along the three spatial directions in the computational domain,

$$\begin{aligned} U &= \xi_x \bar{u}+\xi_y \bar{v}+\xi_z \bar{w},\\ V &= \eta_x \bar{u}+\eta_y \bar{v}+\eta_z \bar{w},\\ W &= \zeta_x \bar{u}+\zeta_y \bar{v}+\zeta_z \bar{w}. \end{aligned} \tag{21}$$

$q=[\bar{u}, \bar{v}, \bar{w}]^T$ is the velocity vector and the vectors E, F and G contain the pressure and viscous terms

$$\begin{aligned} E &= E_p-\frac{\xi_x}{J}E_v-\frac{\xi_y}{J}F_v-\frac{\xi_z}{J}G_v,\\ F &= F_p-\frac{\eta_x}{J}E_v-\frac{\eta_y}{J}F_v-\frac{\eta_z}{J}G_v,\\ G &= G_p-\frac{\zeta_x}{J}E_v-\frac{\zeta_y}{J}F_v-\frac{\zeta_z}{J}G_v, \end{aligned} \tag{22}$$

$$\begin{aligned} E_p &= \frac{1}{J}[\xi_x \bar{p}, \xi_y \bar{p}, \xi_z \bar{p}]^T,\\ F_p &= \frac{1}{J}[\eta_x \bar{p}, \eta_y \bar{p}, \eta_z \bar{p}]^T,\\ G_p &= \frac{1}{J}[\zeta_x \bar{p}, \zeta_y \bar{p}, \zeta_z \bar{p}]^T, \end{aligned} \tag{23}$$

$$E_v=(\nu+\nu_T)\begin{bmatrix} 2(\xi_x \bar{u}_\xi+\eta_x \bar{u}_\eta+\zeta_x \bar{u}_\zeta)\\ \xi_y \bar{u}_\xi+\eta_y \bar{u}_\eta+\zeta_y \bar{u}_\zeta+\xi_x \bar{v}_\xi+\eta_x \bar{v}_\eta+\zeta_x \bar{v}_\zeta\\ \xi_x \bar{w}_\xi+\eta_x \bar{w}_\eta+\zeta_x \bar{w}_\zeta+\xi_z \bar{u}_\xi+\eta_z \bar{u}_\eta+\zeta_z \bar{u}_\zeta \end{bmatrix},$$

$$F_v=(\nu+\nu_T)\begin{bmatrix} \xi_y \bar{u}_\xi+\eta_y \bar{u}_\eta+\zeta_y \bar{u}_\zeta+\xi_x \bar{v}_\xi+\eta_x \bar{v}_\eta+\zeta_x \bar{v}_\zeta\\ 2(\xi_y \bar{v}_\xi+\eta_y \bar{v}_\eta+\zeta_y \bar{v}_\zeta)\\ \xi_z \bar{v}_\xi+\eta_z \bar{v}_\eta+\zeta_z \bar{v}_\zeta+\xi_y \bar{w}_\xi+\eta_y \bar{w}_\eta+\zeta_y \bar{w}_\zeta \end{bmatrix},$$

$$G_v=(\nu+\nu_T)\begin{bmatrix} \xi_x \bar{w}_\xi+\eta_x \bar{w}_\eta+\zeta_x \bar{w}_\zeta+\xi_z \bar{u}_\xi+\eta_z \bar{u}_\eta+\zeta_y \bar{u}_\zeta\\ \xi_z \bar{v}_\xi+\eta_z \bar{v}_\eta+\zeta_z \bar{v}_\zeta+\xi_y \bar{w}_\xi+\eta_y \bar{w}_\eta+\zeta_y \bar{w}_\zeta\\ 2(\xi_z \bar{w}_\xi+\eta_z \bar{w}_\eta+\zeta_z \bar{w}_\zeta) \end{bmatrix}. \tag{24}$$

Here, the velocity gradients are written as $\bar{u}_\xi = \partial\bar{u}/\partial\xi$, etc., and the metrics of the transformation are defined by $\xi_x = \partial\xi/\partial x$, etc.

3. NUMERICAL METHOD

The numerical method developed in this study for LES of incompressible turbulent flows is summarized in this section. The key features of the spatial discretization, the dual time stepping and the pseudo-time convergence acceleration techniques are emphasized.

3.1. Spatial discretization

In order to obtain adequate accuracy for turbulent flow simulations without losing applicability to complex geometry and simplicity of the scheme, Rai and Moin [4] suggested a high-order-accurate, upwind-biased finite difference method. Their approach used a non-conservative form of the unsteady, incompressible Navier–Stokes equations, (2) and (3). Hence, it is appropriate only for simulations of flow fields without discontinuity. The present study is limited to such flows and, therefore, a similar methodology is adopted here.

Similar to Rai and Moin [4], the convective terms are approximated using fifth-order-accurate, upwind-biased finite differences with a seven-point stencil. For example, the first term in the momentum equation, $(U/J)q_\xi$, is evaluated as

$$\left(\frac{U}{J}q_\xi\right)_{i,j,k} = \frac{(U/J)_{i,j,k}}{120}(-6q_{i+2,j,k}+60q_{i+1,j,k}+40q_{i,j,k}-120q_{i-1,j,k}+30q_{i-2,j,k}-4q_{i-3,j,k}) \tag{25}$$

if $U_{i,j,k} > 0$, and

$$\left(\frac{U}{J}q_\xi\right)_{i,j,k} = \frac{(U/J)_{i,j,k}}{120}(4q_{i+3,j,k}-30q_{i+2,j,k}+120q_{i+1,j,k}-40q_{i,j,k}-60q_{i-1,j,k}+6q_{i-2,j,k}) \tag{26}$$

if $U_{i,j,k} < 0$. The remaining convective terms are evaluated in a similar manner.

The viscous terms are computed using central differences. By applying the fourth-order-accurate, half-points differencing, the first viscous term in the u momentum equation, $(c\bar{u}_\xi)_\xi$, where $c = 2(\nu + \nu_T)\xi_x/J$, is discretized as

$$[(c\bar{u}_\xi)_\xi]_{i,j,k} = \frac{1}{24}[-(c\bar{u}_\xi)_{i+3/2,j,k}+27(c\bar{u}_\xi)_{i+1/2,j,k}-27(c\bar{u}_\xi)_{i-1/2,j,k}+(c\bar{u}_\xi)_{i-3/2,j,k}]. \tag{27}$$

Here, $\bar{u}_\xi$, which is defined at the half-points, is computed using the same fourth-order-accurate finite difference given as

$$(\bar{u}_\xi)_{i+1/2,j,k} = \frac{1}{24}(-\bar{u}_{i+2,j,k}+27\bar{u}_{i+1,j,k}-27\bar{u}_{i,j,k}+\bar{u}_{i-1,j,k}). \tag{28}$$

$c_{i+1/2,j,k}$ is interpolated using the information on the same stencil used to evaluated $(\bar{u}_\xi)_{i+1/2,j,k}$ so as to retain high-order accuracy. Thus, the discretization of the viscous terms uses seven grid points and, therefore, the viscous terms are approximated to sixth-order accuracy on uniform grids.

Unlike central difference, all upwind and upwind-biased differences have truncation error terms that are dissipative in nature. In fact, some (low-order) upwind (biased) schemes are

known to be highly dissipative. This can overwhelm the physical dissipation of turbulence and, therefore, needs to be carefully evaluated.

This issue has been addressed in the present study. Figure 1(a) shows the time variation of the turbulent kinetic energy in decaying isotropic turbulence (the description of this flow field will be given later in Section 4.1). Results obtained on a 48^3 grid resolution using fifth-order-accurate upwind-biased finite differences (implemented with and without the LDKM) are shown together with the experimental data. It can be observed that the numerical dissipation of the finite difference scheme is lower than the turbulent dissipation. This is an essential requirement for a turbulence simulation code. As shown, the LES data agree with experimental data only when the SGS model is turned on. This demonstrates the need for and the capability of the SGS model. For comparison, the results without the SGS model obtained using a well-known pseudo-spectral code [15] with a '2/3 dealiasing rule' is also plotted (obtained directly from Figure 1 in Carati *et al.* [30]). Note that the simulation results obtained without a subgrid model should not be considered as DNS since 48^3 grid resolution is too coarse to resolve all the turbulence scales. For example, for this particular case, at least 384^3 grid resolution is required for DNS [16]. The present finite difference method appears to be less dissipative than the spectral method. This is somewhat surprising since the spectral methods are known to be the least dissipative methods available for turbulence simulation. However, this may be due to some small deviations in the initial energy distribution (in the spectral space) between the current physical implementation and Carati *et al.*'s initialization in spectral space. Nevertheless, it can be concluded that the dissipation of the present finite different method is at least comparable with that of the spectral scheme and, therefore, is acceptable for turbulence flow simulations.

Figure 1(b) shows the unscaled energy spectra at two instants in time, $t^* = 4.98$ and $t^* = 8.69$ (here, t^* denotes the dimensionless time as defined later in Section 4.1) obtained in decaying isotropic turbulence with and without the LDKM. Without the model, energy builds up at the high wavenumber end by $t^* = 4.98$ and as time evolves, the prediction without the model worsens at all wavenumbers. This result again suggests that the present algorithm has the requisite properties for use in DNS and LES.

Note that if a non-staggered grid is used, and the velocity derivatives in the continuity equation and the pressure derivatives in the momentum equation are central-differenced, velocity and pressure are decoupled. This decoupling generates undesirable grid-scale (odd–even) oscillations in the pressure field. Some higher-order artificial dissipation terms are typically needed to eliminate the pressure oscillations. However, artificial dissipation terms need to be avoided in turbulence simulations since they may contaminate the simulated flow field. On the other hand, a staggered grid method originally proposed by Harlow and Welch [31] can be used to avoid the pressure oscillations. However, this method requires more care when used with non-rectangular geometry and non-uniform grids. It also requires some special treatment at boundaries. When a non-staggered grid is used, the pressure oscillations can be eliminated by using special interpolation techniques, such as momentum interpolation [32] and elliptic-corrected linear interpolation [33] techniques. Strikwerda [34] used the central difference scheme with the addition of regularizing terms for the pressure gradient and divergence operators (hence, it is called the regularized central difference). The regularizing terms ensure proper coupling between the pressure and the velocity fields. In this scheme, the pressure derivatives are approximated as

$$\frac{\partial p}{\partial x} \simeq \delta_x p - \alpha \Delta_x^2 \delta_{x-} \delta_{x+}^2 p, \tag{29}$$

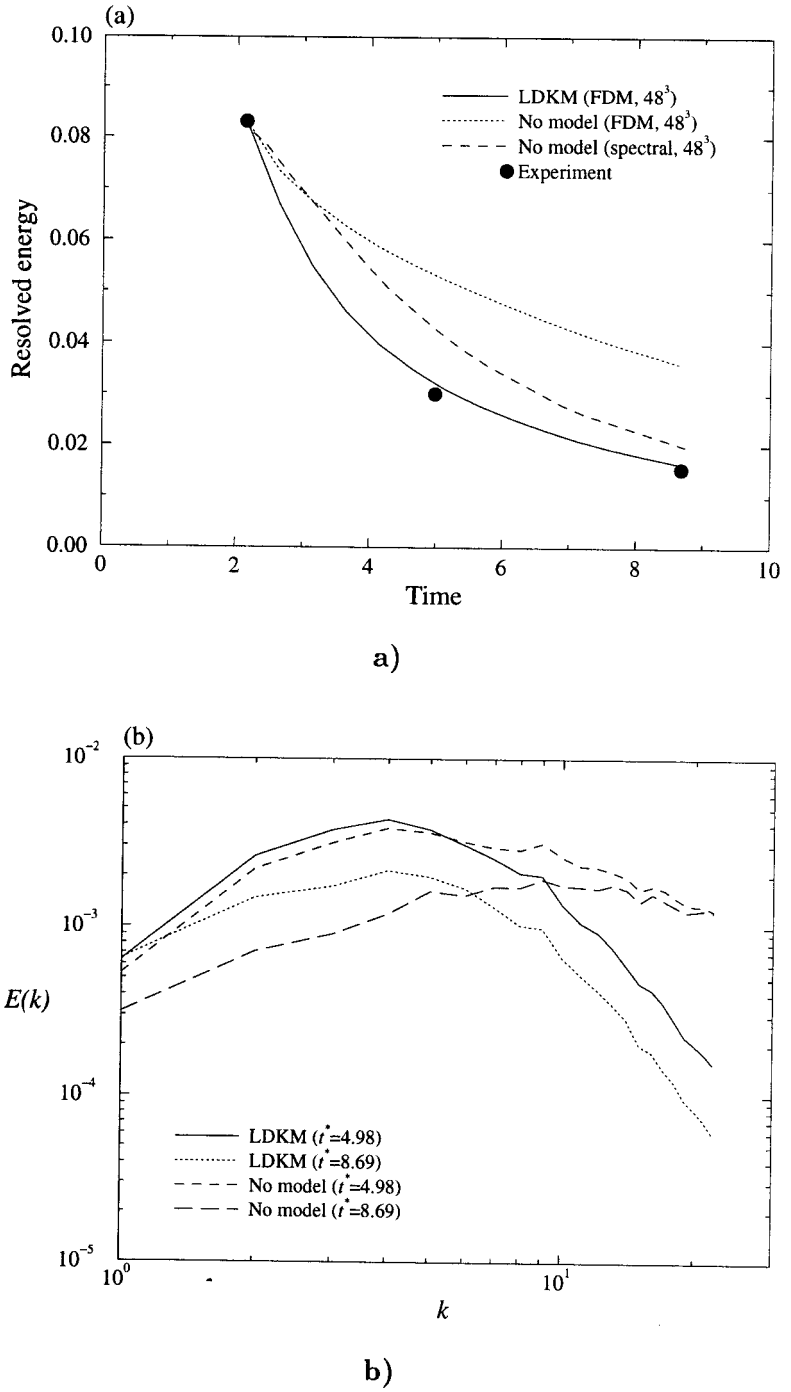

Figure 1. (a) Decay of resolved turbulent kinetic energy and (b) energy spectra in decaying isotropic turbulence. Spectral code results of Carati *et al.* [30] (no model case) and experimental data of Comte-Bellot and Corsin [47] are also plotted in (a).

and the velocity derivatives in the continuity equation are approximated as

$$\frac{\partial u}{\partial x} \simeq \delta_x u - \alpha \Delta_x^2 \delta_{x+} \delta^2_{x-} u, \tag{30}$$

where α is a non-zero constant and δ_x, δ_{x+} and δ_{x-} are the central, forward and backward difference operators respectively. For $\alpha = \frac{1}{6}$, Equations (29) and (30) are third-order accurate. In the present study, a similar scheme is adopted. However, to prevent the degradation of accuracy, fifth-order-accurate approximations are used. For instance,

$$\left[\left(\frac{\xi_x \bar{p}}{J}\right)_\xi\right]_{i,j,k} = \frac{1}{120}\left[4\left(\frac{\xi_x \bar{p}}{J}\right)_{i+3,j,k} - 30\left(\frac{\xi_x \bar{p}}{J}\right)_{i+2,j,k} + 120\left(\frac{\xi_x \bar{p}}{J}\right)_{i+1,j,k} - 40\left(\frac{\xi_x \bar{p}}{J}\right)_{i,j,k} - 60\left(\frac{\xi_x \bar{p}}{J}\right)_{i-1,j,k} + 6\left(\frac{\xi_x \bar{p}}{J}\right)_{i-2,j,k}\right], \tag{31}$$

$$\left[\left(\frac{U}{J}\right)_\xi\right]_{i,j,k} = \frac{1}{120}\left[-6\left(\frac{U}{J}\right)_{i+2,j,k} + 60\left(\frac{U}{J}\right)_{i+1,j,k} + 40\left(\frac{U}{J}\right)_{i,j,k} - 120\left(\frac{U}{J}\right)_{i-1,j,k} + 30\left(\frac{U}{J}\right)_{i-2,j,k} - 4\left(\frac{U}{J}\right)_{i-3,j,k}\right]. \tag{32}$$

Note that the regularized central difference scheme is a variant of the central difference scheme and, hence, the biasing of the scheme does not depend on the direction of the local contravariant velocity.

The accuracy and the effect of the non-symmetric regularizing terms on the turbulence statistics have been examined by simulating decaying isotropic turbulence and comparing the results with those obtained using the following fourth-order-accurate (non-regular) central differences

$$\left[\left(\frac{\xi_x \bar{p}}{J}\right)_\xi\right]_{i,j,k} = \frac{1}{12}\left[-\left(\frac{\xi_x \bar{p}}{J}\right)_{i+2,j,k} + 8\left(\frac{\xi_x \bar{p}}{J}\right)_{i+1,j,k} - 8\left(\frac{\xi_x \bar{p}}{J}\right)_{i-1,j,k} + \left(\frac{\xi_x \bar{p}}{J}\right)_{i-2,j,k}\right], \tag{33}$$

$$\left[\left(\frac{U}{J}\right)_\xi\right]_{i,j,k} = \frac{1}{12}\left[-\left(\frac{U}{J}\right)_{i+2,j,k} + 8\left(\frac{U}{J}\right)_{i+1,j,k} - 8\left(\frac{U}{J}\right)_{i-1,j,k} + \left(\frac{U}{J}\right)_{i-2,j,k}\right]. \tag{34}$$

Figure 2 shows the comparison for the time evolution of the turbulent kinetic energy (Figure 2(a)) and unscaled energy spectra (Figure 2(b)). As shown, almost identical results have been obtained using both types of central difference schemes. This result demonstrates the accuracy of the regularized central differences and the negligible effect of the scheme bias on the turbulence statistics.

3.2. Dual time stepping

The major difference between incompressible and compressible Navier–Stokes formulations is the lack of a time derivative term in the continuity equation in the incompressible formulation. Therefore, satisfying the mass conservation equation is the primary issue in solving the incompressible equations. Physically incompressible flow is characterized by the elliptic behavior of the (infinitely fast) pressure waves. Since the pressure field is part of the solution, various primitive variable formulations, such as the marker and cell (MAC) method [31], the fractional step (or the projection) method [35], and the artificial compressibility method [36], have been developed. However, to the authors' best knowledge no method has been proven superior for general flow problems.

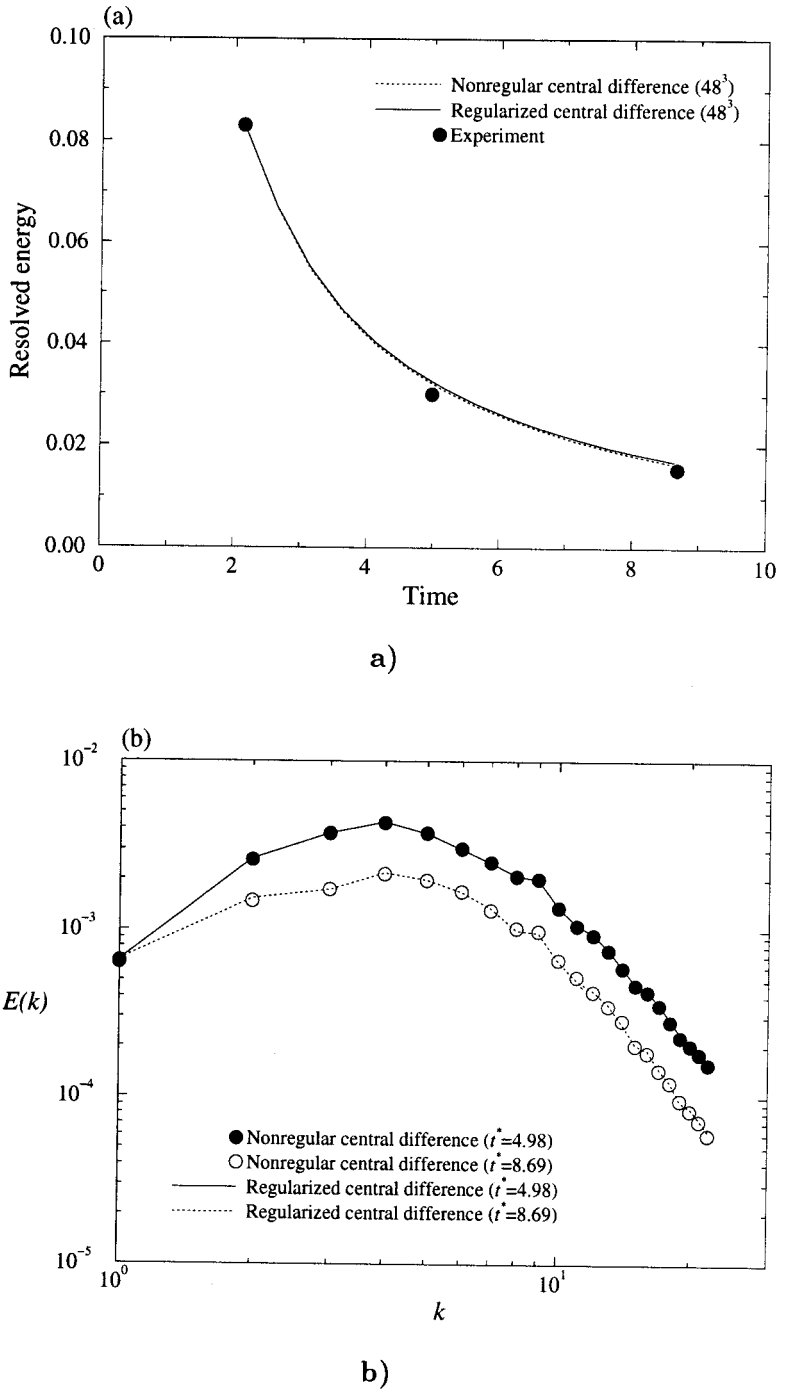

Figure 2. Comparison between the regularized central differences and the non-regular central differences using the decaying isotropic turbulence results. (a) Decay of resolved turbulent kinetic energy and (b) energy spectra. Experimental data of Comte-Bellot and Corsin [47] are also plotted in (a).

In the present study, the artificial compressibility method (which was originally suggested by Chorin [36]) is adopted. The main advantage of this approach is that by introducing artificial unsteady terms into the continuity equation, efficient solution algorithms developed for time-dependent compressible flows can be utilized to compute incompressible flows. In this formulation, the continuity equation is modified by adding a pseudo-time derivative of the pressure term, which results in hyperbolic–parabolic time-dependent equations together with the unsteady momentum equations,

$$\frac{\partial p}{\partial \tau} = -\beta^2 J\left[\frac{\partial}{\partial \xi}\left(\frac{U}{J}\right)+\frac{\partial}{\partial \eta}\left(\frac{V}{J}\right)+\frac{\partial}{\partial \zeta}\left(\frac{W}{J}\right)\right]. \tag{35}$$

Here, β is a prescribed parameter that represents an artificial speed of sound and reduces the stiffness of the equations, and τ is the pseudo-time variable which is not related to the physical time t. The choice of β is crucial in determining convergence and stability properties of the numerical scheme. Since β has the dimension of a speed, it cannot be a universal constant. For instance, if the non-dimensionalized governing equations are employed, β is non-dimensionalized by a reference velocity. Therefore, the optimal β will depend on the choice of the reference velocity. Some researchers [37] chose β^2 to be slightly larger than $\bar{u}^2+\bar{v}^2+\bar{w}^2$ as an optimal choice. However, in general, the superiority of this choice of β over a constant β has not yet been proven. McHugh and Ramshaw [38] found that for a large time step the fastest convergence is obtained by using the conventional value of ($\beta^2 \sim \bar{u}^2+\bar{v}^2+\bar{w}^2$). However, in contrast, the fastest convergence for a small time step is obtained by letting β be much larger than the conventional value. Based on this observation, they proposed a simple analytical expression for β as function of the time step. In the present study, both a constant β and a variable β, i.e. $\beta^2 = C(\bar{u}^2+\bar{v}^2+\bar{w}^2)$ (where C is a constant of order unity) have been evaluated. It was concluded that for most of the problems studied here, a constant β provided better convergence. Based on the numerical experiments, Marx [39] concluded similarly that optimal convergence rate is obtained when β^2 is estimated from the maximum of $C(\bar{u}^2+\bar{v}^2+\bar{w}^2)$ (i.e. β is constant) in the flow fields. He also estimated C to be close to 3.

Figure 3 shows a typical example of the pseudo-time convergence for one physical time step advance for various values of β. The decaying isotropic turbulence is solved on a 48^3 grid resolution using a two-level multigrid, CFL = 2, and a physical time step equal to 0.05. For this test case, the choice of $\beta^2 \approx 20$ gives optimum performance. The maximum of $(\bar{u}^2+\bar{v}^2+\bar{w}^2)$ is about 3 in the initial flow field. Therefore, optimal C is greater than 6, which is much larger than the value suggested by Marx [39]. The reason for the larger value of optimal C is the fact that relatively small time steps are used for the present numerical experiment to ensure time accuracy.

Pseudo-time velocity derivatives are also added to the momentum equations [1] to obtain the artificial compressibility form of the equations. Thus,

$$\frac{\partial q}{\partial \tau} = -\frac{\partial q}{\partial t} - R^*(q) = -R(q), \tag{36}$$

where R^* represents the residual in the momentum equations, which includes convective and viscous terms. In this formulation, the governing equations are marched in the pseudo-time (i.e. subiterated) until the divergence-free flow field is obtained. Therefore, artificial compressibility does not corrupt the physical time solution as long as the pseudo-time solution converges to a steady state at each physical time level.

The integration in the pseudo-time is carried out by a five-stage Runge–Kutta time stepping scheme. If m is the index associated with pseudo-time, this scheme can be written in the form

$$q^{(0)} = q^m,$$
$$q^{(k)} = q^{(0)} - \alpha_k \Delta\tau R(q^{(k-1)}), \quad k = 1 \ldots 5,$$
$$q^{m+1} = q^{(5)}. \tag{37}$$

Here, the coefficients are chosen as $\alpha_1 = 0.059$, $\alpha_2 = 0.145$, $\alpha_3 = 0.273$, $\alpha_4 = 0.5$ and $\alpha_5 = 1.0$, which are considered appropriate for the upwind scheme [13].

The physical time derivatives in the momentum equations are computed using a second-order backward difference that results in an implicit scheme,

$$\frac{\partial q}{\partial \tau} = -\frac{3q^{n+1} - 4q^n + q^{n-1}}{2\Delta t} - R^*(q^{n+1}) = -R(q^{n+1}), \tag{38}$$

where the superscript n denotes the physical time level. This backward differencing scheme is strongly stable and dissipative and thus it is nearly insensitive to the stiffness of the problem. This characteristic of the scheme can enhance the applicability of the scheme to any stiff problem. However, at the same time, it can also degrade the time accuracy of the scheme. Therefore, the time step must be chosen carefully to ensure the adequate time accuracy. Instead of using this type of dissipative time integration, one may use the Crank–Nicolson scheme which is non-dissipative. Only dispersion errors are significant in such a scheme and these errors usually grow with increasing time step. Therefore, the time step is limited by stability considerations and furthermore, this scheme is very sensitive to the type of flow field. Marx [39] tested both these schemes and concluded that the backward differencing scheme provided a much better performance for unsteady flows driven by fast transient but the Crank–Nicolson scheme was better for a free vortex shedding problem. Based on this observation, he proposed an implicit Runge–Kutta scheme that performed well for both test problems. This implicit Runge–Kutta scheme typically requires more subiterations for the

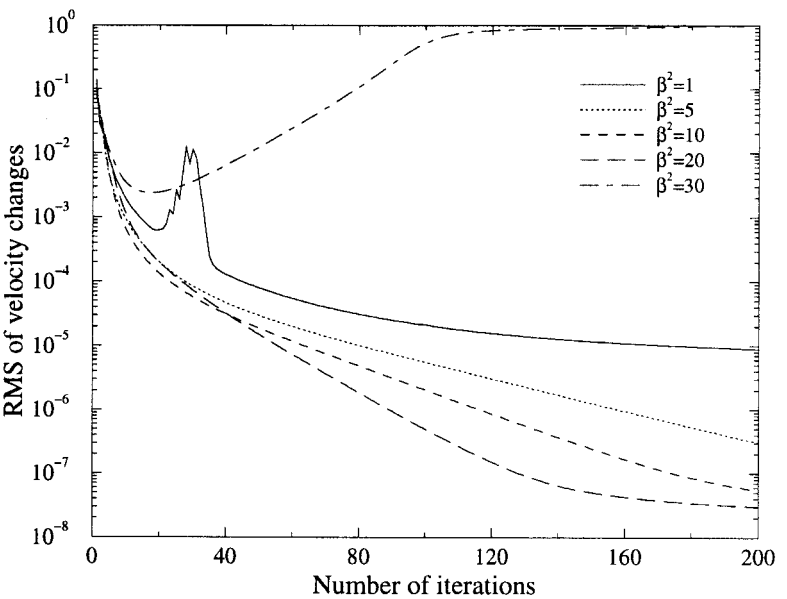

Figure 3. Pseudo-time convergence history for variation of β during one physical time step advance in decaying isotropic turbulence simulation.

same time step to reach the pseudo-time steady state than the backward differencing scheme. Furthermore, the applicability of this scheme to unsteady turbulent flows has not yet been established. Therefore, the present approach employs the backward differencing scheme and the time step is chosen small enough so as to ensure that time accuracy is not compromised.

3.3. Convergence acceleration techniques

To accelerate the convergence in pseudo-time marching at each physical time step, efficient acceleration techniques developed for explicit steady state solvers, such as local time stepping, residual smoothing and multigrid, are employed. Local time stepping involves using the locally maximum allowable time step. The local time step for viscous flow can be computed as [40]

$$\Delta\tau = \mathrm{CFL}\,\frac{1}{\lambda_\xi + \lambda_\eta + \lambda_\zeta + 2(\nu + \nu_T)J^2(S_\xi^2 + S_\eta^2 + S_\zeta^2)}, \tag{39}$$

where CFL is the Courant–Friedrichs–Lewy number, λ_ξ, λ_η and λ_ζ are the spectral radii in the ξ-, η- and ζ-directions, given as

$$\begin{aligned}
\lambda_\xi &= |U| + \beta(\xi_x^2 + \xi_y^2 + \xi_z^2)^{1/2},\\
\lambda_\eta &= |V| + \beta(\eta_x^2 + \eta_y^2 + \eta_z^2)^{1/2},\\
\lambda_\zeta &= |W| + \beta(\zeta_x^2 + \zeta_y^2 + \zeta_z^2)^{1/2},
\end{aligned} \tag{40}$$

where $S_\xi^2 = x_\xi^2 + y_\xi^2 + z_\xi^2$, etc. Note that the local time step $\Delta\tau$ must be less than the physical time step Δt to make the scheme stable.

The stability limit of the basic scheme can be extended by employing residual smoothing [41]. In three dimensions, an implicit residual smoothing is carried out in the following form

$$(1 - \epsilon_x\delta_x^2)(1 - \epsilon_y\delta_y^2)(1 - \epsilon_z\delta_z^2)\tilde{R} = R, \tag{41}$$

where ϵ_x, ϵ_y and ϵ_z are smoothing coefficients and δ_x^2, δ_y^2 and δ_z^2 are central difference operators in the x-, y- and z-directions. R and $\tilde{R}$ are the residuals before and after smoothing. Thus, each residual is replaced by an average of itself and the neighboring residuals. In most cases, with residual smoothing, a CFL of 5 was possible for the pseudo-time iteration.

Convergence can also be further accelerated by incorporating the full approximation storage (FAS) scheme based multigrid method as proposed by Brandt [42] and further developed by Jameson [41]. The basic idea is to solve the governing equations on a sequence of successively coarser grids to speed up the propagation of the fine grid corrections. This has two advantages. First, the computational effort per time step is reduced on a coarser grid. Second, the use of coarser grids tracks the evolution on a larger scale, with the consequence that global equilibrium can be more rapidly attained. In the case of an explicit time stepping scheme, this manifests itself as successively larger time steps as the solution procedure moves to coarser grids without violating the stability limit. Auxiliary coarser grids are introduced by doubling the grid spacing. The FAS multigrid method is not illustrated here for brevity, since the detailed description of the method can be found in numerous published works [41,42].

It is worth noting that the success of the multigrid method is critically dependent upon the choice of the restriction and prolongation operators (i.e. information transfers between grid levels). If the errors due to either the restriction or the prolongation procedure are significant, then the convergence will be seriously impaired. In general. the prolongation operator does not have to be the exact inverse of the restriction operator. Moreover, the restriction operator for the solution and for the residual need not be the same. In the present study, point-to-point

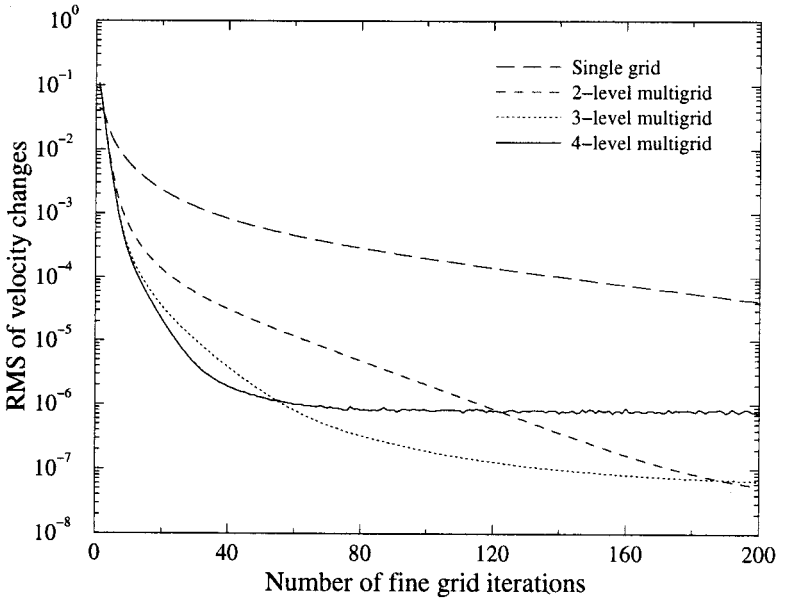

Figure 4. Pseudo-time convergence history for variation of multigrid levels during one physical time step advance in decaying isotropic turbulence simulation.

injection [13] is used for restricting the solution while a volume-weighted average over the neighboring 27 points is used for residual restriction. The corrections are prolonged back to the finer grid by bilinear interpolation.

The treatment of the boundary conditions on the coarser grids also influences the multigrid convergence. In the present study, the boundary conditions are imposed in the same way on each grid and updated at every Runge–Kutta stage. The turbulent eddy viscosity on coarse grids is evaluated by injecting the SGS turbulent kinetic energy and the dynamically determined model coefficients from the fine grid instead of solving the transport equation on the coarse grids. Earlier, results obtained using this approach was compared with results obtained when the SGS kinetic energy was directly computed on each coarse grid. Comparison of the two methods showed no observable differences. Therefore, for computational expediency, the former method was employed for the simulations reported here. It is likely that the latter method may be needed in more complex flow problems. This requirement if needed can be easily incorporated in the present method.

The pseudo-time convergence history during one physical time advance for the four different multigrid level cases is compared in Figure 4. Again, decaying isotropic turbulence is solved on a 48^3 grid resolution using $\beta^2 = 10$, CFL = 2 and a physical time step equal to 0.05. As shown, increasing the number of multigrid levels from 1 to 3 shows an improvement in convergence. However, beyond three multigrid levels, the convergence saturates earlier. This earlier convergence saturation seems to be related to the fact that 6^3 and 12^3 grid resolutions are too coarse to provide the accurate corrections for a very small velocity change.

In practice, a solution is considered converged if the root-mean-square of pressure and velocity changes decrease less than 10^{-6} since, in most cases, further iterations to reduce these quantities do not noticeably change the solution. Both the eddy viscosity and the model coefficients are computed at each pseudo-time step. Usually, the model coefficients adjust themselves quickly and remain almost constant during pseudo-time iterations.

The efficiency of the present numerical method has been evaluated by simulating the lid-driven cavity (recirculating) flow (the detailed description of the flow field is given in Section 4.6) on 32^3 grid, and comparing the CPU and memory usage with data obtained using other numerical methods for the same test case. Existing schemes include two staggered grid methods, one explicit and one fully implicit, and one non-staggered grid method by Zang *et al.* [3], which employs a semi-implicit fractional step approach. The comparison is summarized in Table I for the CPU time (in μs) per grid point per time step and the number of three-dimensional variables defined per grid point. All three existing schemes' data have been adopted from Zang *et al.*'s paper [3] and their CPU time has been measured on a Cray Y-MP 8/864 supercomputer. However, the present computation was carried out on a single processor SGI Power Challenge (75 MHz). Therefore, the CPU time cannot be directly compared. Rather, an approximate comparison based on the reported benchmark is carried out. Saini and Bailey [43] performed a benchmark test of a simplified multigrid kernel, which solves a three-dimensional Poisson partial differential equation (PDE). They obtained the speed ratio of SGI Power Challenge (90 MHz) with respect to Cray Y-MP equals to 0.45 when both ran on eight processors. Using this result, we calibrate/rescale the present study's result and determine a CPU time of 100 μs for the present solver (as shown in Table I) on 75 MHz Power Challenge is equivalent to 38 μs on a Cray Y-MP, which compares very well to the Y-MP CPU time obtained in the fractional step method of Zang *et al.* [3].

For the above comparison, the time step was chosen based on the CFL condition to best match the time step of Zang *et al.* [3]. In the present case, typically two to three subiterations were required to complete one physical time step after the non-physical initialization effects were washed out. The fractional step method employs a semi-implicit scheme and, therefore, the admissible time step is restricted by stability restriction. In contrast, the present (fully implicit) time integration scheme can use a larger time step than dictated by the CFL condition (since the time step of the present scheme is only restricted by accuracy considerations). Furthermore, as observed by Marx [39] and confirmed by the present authors (not shown), the number of subiterations needed to achieve the pseudo-steady state is insensitive to the (physical) time step size. Hence, if the comparison is made in terms of the absolute computational cost to achieve a time-accurate solution over a fixed physical time period, the present solver may be relatively more efficient.

The total number of the three-dimensional variables per grid point, as shown in the table, can also be significantly reduced in the non-staggered grid methods in comparison with the staggered grid methods. Thus, the present algorithm appears to be computationally efficient (both in terms of memory requirement and CPU time needed) when compared with alternate methods reported in the literature.

Table I. Comparison of CPU time per grid point per time step and number of three-dimensional variables per grid point between the present method and existing incompressible methods

	CPU time (μs)	Number of variables
Explicit staggered grid [3]	60 (Y-MP 8/864)	103
Implicit staggered grid [3]	110 (Y-MP 8/864)	94
Fractional step [3]	28 (Y-MP 8/864)	51
Artificial comp. (present)	100 (SGI Power Challenge 75 MHz)	36

4. RESULTS AND DISCUSSIONS

To validate the LES solver developed in this study, we have implemented *a posteriori* tests of decaying (Section 4.1), forced (Section 4.2) and rotating (Section 4.3) isotropic turbulent flows, temporally evolving turbulent mixing layers (Section 4.4), turbulent plane Couette flows (Section 4.5) and turbulent recirculating flows (Section 4.6). These test flows were chosen to evaluate the present method under various conditions of increasing complexity. Comparisons with experimental data and DNS results (wherever available) are carried out to demonstrate the capability of the code. Results of some of the present LES are also compared with LES results (wherever available) obtained using other subgrid models [30,44].

Before presenting the results, it is worthwhile to discuss grid independence studies that are required to establish the accuracy of the solution. In conventional steady state approaches, grid-independent studies primarily address whether geometry-dependent large-scale motions are properly resolved. However, in LES, full resolution of these large-scale motions is a prerequisite, by definition. Therefore, grid convergence studies of LES need to be interpreted differently from conventional steady state studies. LES results obtained using different grid resolutions resolve different amounts of turbulent kinetic energy and all these results are equally accurate as long as the grid employed is larger than the grid required to resolve the relevant large scales. This is demonstrated in the following section where three different grid resolution LES of decaying isotropic turbulence show different results but match well with experimental data (when they are also resolved on the same grid).

Most eddy viscosity based SGS models are known to approximate correctly the isotropic components of the subgrid stress tensor (which determine the rate of energy dissipation). However, most models correlate poorly with the anisotropic components of the subgrid-scale stress tensor [14,19]. Therefore, anisotropic components of the subgrid stress tensor should be resolved explicitly by the grid resolution. For flows without mean shear such as isotropic turbulence (which can be fully characterized by the rate of energy dissipation), the grid resolution requirement depends only on the quality of the employed SGS model. If a more accurate and physically accurate SGS model is employed, a coarser grid can be used. As is demonstrated in the following section, the LDKM works reasonably well in isotropic turbulence up to the grid resolution, where almost half of turbulent kinetic energy remains unresolved. However, for wall-bounded flows where a wide range of anisotropic small scales are generated near walls, the adequate resolution is determined by the size of these anisotropic scales. Baggett *et al*. [45] studied this issue and provided an estimate for the near wall layer resolution requirement. In this study, the required resolution was determined in *a posteriori* manner by checking the accuracy of the simulated wall layer. These issues are discussed later. Unless otherwise noted, most of the results presented here were obtained using the minimum number of grid points required to achieve accurate results.

4.1. Decaying isotropic turbulence

In turbulent flow simulations, it is very difficult to measure the time accuracy from instantaneous flow data, since two different turbulent flows with a small discrepancy in the initial state (e.g. the initial random seed) will evolve in a totally different manner even though both of them may represent evolution of realistic turbulence. Statistical measure of the turbulence evolution may be the only feasible approach to evaluate time accuracy of turbulent simulations [46]. A flow where time accuracy can be evaluated from the results is decaying isotropic turbulence. Therefore, the decaying isotropic turbulence experiment of Comte-Bellot

and Corsin [47] is simulated here. In the experiment, measurements of the energy spectra were carried out at three locations downstream of the grid (which generated the turbulence in the wind tunnel). The spatial evolution of turbulence in this flow can be simulated using a temporal simulation (provided Taylor's frozen turbulence hypothesis is valid, which is the case here). Good agreement of the predicted temporal energy decay rate with the measured spatial energy decay rate can be used to prove the time accuracy of the solver as well as the ability of the SGS model to represent accurately the effect of the unresolved scales. Therefore, this flow has been an ideal test problem that has been utilized by many researchers [21,25,30,48] to evaluate both the numerical scheme and SGS closure models.

Decaying isotropic turbulence inside a cubical box moving with the mean flow velocity is simulated here. The size of the box is chosen to be greater than the integral length scale of the measured real turbulence. The statistical properties of turbulence inside the box are believed to be realistic even after applying periodic boundary conditions for numerical implementation. All experimental data are non-dimensionalized by the reference length scale $10M/2\pi$ (where $M = 5.08$ cm is the mesh size of the grid) and by a reference time scale 0.1 s (chosen for computational convenience). Using this non-dimensionalization, the three locations where the experimental data were measured correspond to the three dimensionless time levels $t^* = 2.13$, 4.98 and 8.69 respectively. At the first measuring station, the Reynolds number based on the Taylor microscale Re_λ and the integral scale Re_ℓ were respectively 71.6 and 187.9 (these values decreased to 60.7 and 135.7 respectively at the last measuring station).

The initial velocity field (primarily the amplitudes of the velocity Fourier modes) is chosen to match the three-dimensional energy spectrum at the first experimental station. The phases of Fourier modes are chosen to be random so that the initial velocity field satisfy Gaussian statistics. The initial pressure is assumed to be uniform throughout the flow field and the initial SGS kinetic energy is estimated by assuming similarity between the SGS kinetic energy and the resolved-scale kinetic energy at the test filter level. Thus, at $t^* = 2.13$, we chose

$$k_{\mathrm{SGS}} \approx \frac{C_k}{2}(\widehat{\bar{u}_k\bar{u}_k} - \hat{\bar{u}}_k\hat{\bar{u}}_k), \tag{42}$$

where the constant C_k is determined by matching the total amount of k_{SGS} with the exact amount of the kinetic energy remaining above the cut-off wavenumber at the first location in the experiment. Because the initial flow field is not real turbulence, realistic energy decay occurs only after some adjustment period, which takes a few time steps in the actual simulation.

Figure 5 shows the decay of the resolved turbulent kinetic energy computed using the present solver using three grid resolutions, 48^3, 32^3 and 24^3. The results are compared with the experimental data of Comte-Bellot and Corsin [47]. The predictions of LES are in good agreement with the experiment. Even when 24^3 grid is employed (which implies that a significant amount, nearly half, of the subgrid kinetic energy remains unresolved), the present LDKM model LES gives reasonably good agreement.

As is well known, the turbulent kinetic energy undergoes a power law decay, i.e. $E \sim (t^*)^a$, in the asymptotic self-similar regime. Table II shows this decay exponent a which is obtained from a least-square fit to each data. The results predicted by the other models (DSM, DLM(k) and DLM(S)) are also shown in the table as given in Carati *et al.* [30]. Here, DSM, DLM(k), and DLM(S) denote respectively the dynamic Smagorinsky model by Germano *et al.* [8], the dynamic localization model by Ghosal *et al.* [48], and the stochastic dynamic localization model by Carati *et al.* [30]. These results confirm the agreement between the LES and the experiment. More importantly, the present results at all three grid resolutions used show consistency in predicting the energy decay accurately.

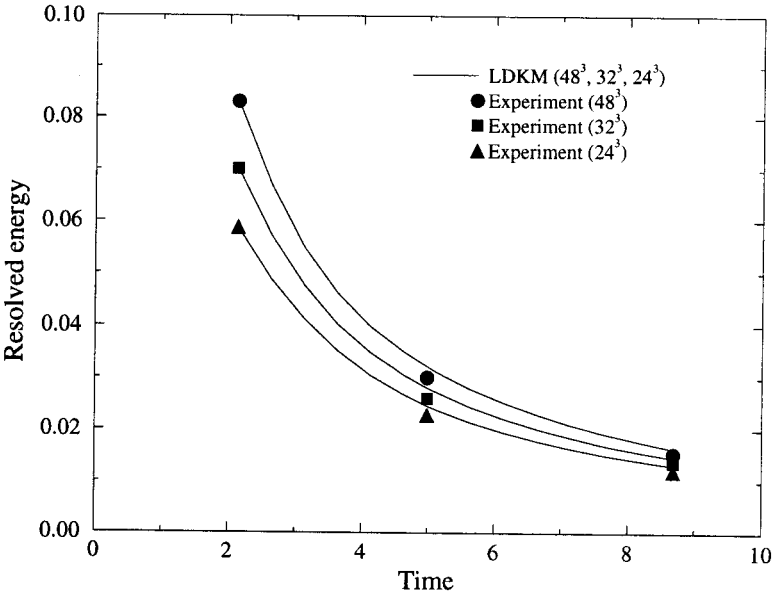

Figure 5. Decay of turbulent kinetic energy in isotropic turbulence, resolved by LES with three different grid resolutions. Experimental data of Comte-Bellot and Corsin [47] are also plotted.

4.2. Forced isotropic turbulence

A statistically stationary isotropic turbulence is simulated using a 32^3 grid resolution. The results are compared with existing high resolution DNS data by Vincent and Meneguzzi [49] and Jimenez *et al.* [50] obtained at $Re_\lambda \approx 150$ and $Re_\lambda \approx 170$ respectively. A statistically stationary turbulent field is obtained by forcing the large scales as done by Kerr [51] by keeping the initial value of all Fourier modes with wavenumber components equal to 1 fixed. The initial condition is obtained by generating a random realization of the energy spectrum [52].

$$E(k) = C \frac{k^4}{1 + (k/k_0)^{5/3+4}}, \tag{43}$$

where k is a wavenumber, $k_0 = 1$ and C is a constant that normalizes the initial total energy to be 0.5.

Table II. Decay exponent a of the power law decay $E \sim (t^*)^r$ in isotropic turbulence

Grid resolution	48^3	32^3	24^3
Experiment	−1.20	−1.16	−1.12
LDKM	−1.17	−1.13	−1.09
DSM	−1.27		
DLM(k)	−1.28		
DLM(S)	−1.17		

Experimental data are computed from the energy spectra given by Comte-Bellot and Corsin [47]. Results of DSM, DLM(k) and DLM(S) are adopted from Carati *et al.* [30].

Table III. Higher-order moments of the u velocity component in forced isotropic turbulence

	S_4	S_6
512^3 DNS ($Re_\lambda \approx 170$)	2.80	12.5
32^3 LDKM ($Re_\lambda \approx 260$)	2.78	11.9
32^3 LDKM ($Re_\lambda \approx 80$)	2.80	12.1
Gaussian	3.0	15.0

The nth-order moments are denoted by S_n. Results of the 512^3 DNS of Jimenez *et al.* [50] are also included.

Two different flow conditions were simulated. In one case, $Re_\lambda \approx 260$, $Re_\ell \approx 2400$ and $\tau_e \approx 3.7$, while for the second case, $Re_\lambda \approx 80$, $Re_\ell \approx 220$ and $\tau_e \approx 4$. Here Re_λ, Re_ℓ and τ_e, respectively denote the Taylor microscale Reynolds number, the integral scale Reynolds number and the large eddy turnover time (defined by the ratio between the integral scale and the turbulence intensity). The precise (but well known) definitions of these parameters in terms of the wavenumber and the energy dissipation rate are given elsewhere [52]. The simulations were carried out for 27 and 25 large eddy turnover times respectively. To ensure statistical independence, 20 instantaneous fields are used for statistical analysis for both cases with the time interval between successive fields larger than (or at least the same as) one large eddy turnover time.

Figure 6(a) shows the probability distribution of velocity differences, $\delta u(r) = \bar{u}(x+r) - \bar{u}(x)$, for various values of length scale r (note that all values of r used here are comparable with the inertial range scales). Here δu is normalized so that $\sigma^2 = \widetilde{\delta u^2} = 1$ (here '$\sim$' denotes ensemble averaging). The LES results (using the LDKM at $Re_\lambda \approx 260$) clearly show that the distribution changes from a non-Gaussian (which has tails) to a Gaussian, as r increases. The same behavior was observed in the DNS database of Vincent and Meneguzzi [49]. In addition to this agreement, the LES accurately predicts the probability of each bin. Figure 6(b) shows that there is a good agreement between the DNS and LES distributions for $r = 0.39$ obtained, except for deviation in the tail regions. However, as is well known, the tails of the non-Gaussian distribution develop mainly due to small-scale fluctuations. Therefore, the deviation between the LES and the DNS results in the tails is somewhat natural since in LES, the small scales are not resolved, and even the resolved portion of small scales lies under strong influence of the top-hat filter implicitly adopted in the present code.

The statistics of velocity (which are the property of the large scales and mostly resolved in LES) are also investigated. We compute the nth-order moments of the u velocity component distribution using

$$S_n = \frac{\widetilde{u^n}}{\widetilde{u^2}^{n/2}}. \tag{44}$$

The results of these calculations are summarized in Table III. The results of the 512^3 DNS ($Re_\lambda \approx 170$) are obtained from the paper by Jimenez *et al.* [50]. As shown in the table. the velocity statistics predicted by the LES agree well with the DNS results.

4.3. Rotating isotropic turbulence

The principal effect of system rotation on isotropic turbulence is to alter the non-linear interactions among turbulence scales. The system rotation inhibits energy transfer from large

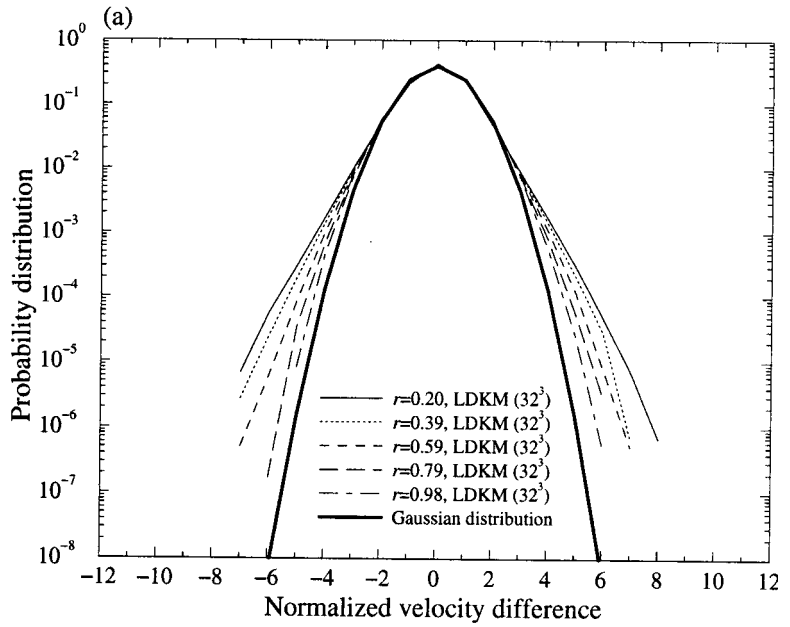

a)

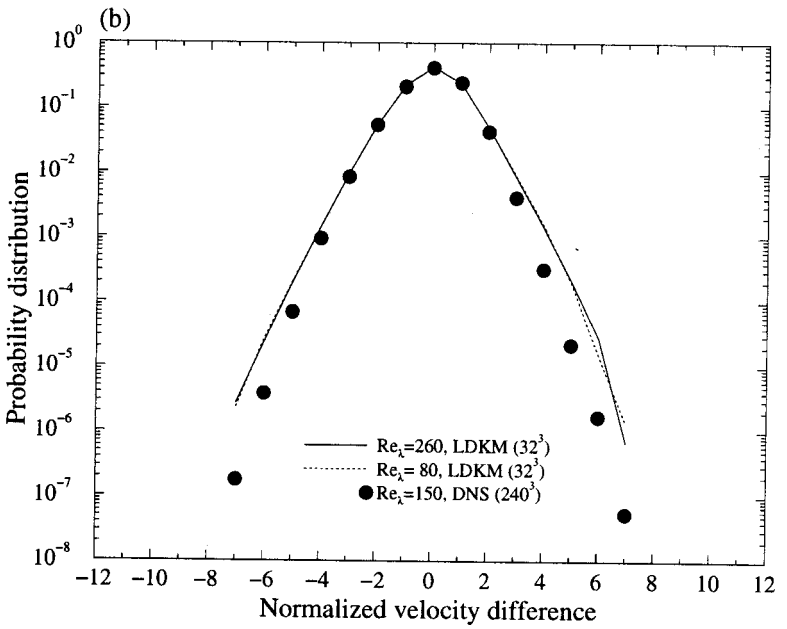

b)

Figure 6. Probability distribution of normalized velocity difference for (a) five different scales (r) and (b) $r = 0.39$ predicted by LES of forced isotropic turbulence. High resolution DNS results of Vincent and Meneguzzi [49] are also plotted in (b).

to small scales and thus leads to a reduction in turbulence dissipation and an associated decrease in the decay rate of turbulence energy. This particular feature is a good test to address the capability of the LDKM approach. In this study, we simulate the experiment of Jacquin *et al.* [53]. The effect of system rotation on the large-scale velocity field can be easily included by adding a Coriolis term to the right-hand side of (3): $2\epsilon_{ij3}\Omega\bar{u}_j$, where ϵ_{ijk} is Levi–Civita's alternating tensor. The resulting equations represent the governing equations of large-scale motions in a reference frame rotating with constant angular velocity Ω about the z-axis. Four different cases, $\Omega = 0$, 15.7, 31.4 and 62.8 rad s^{-1}, were simulated using the 32^3 grid resolution.

The initial field is the same as the one used earlier for the decaying isotropic turbulence simulations described in Section 4.1. The total energy and the time scale of this initial state have been scaled to match those of the experiment of Jacquin *et al.* [53] at the imaginary origin of realistic turbulence where the grid wakes are believed to completely mix together. The imaginary origin is assumed to be $x/M = 2.6$ (M denotes the mesh size of the grid) as given by the authors for $\Omega = 0$ rad s^{-1} and $M = 1.5$ cm.

In Figure 7, the decay of the resolved-scale turbulent kinetic energy, for various rotation rates are compared to the experimental data of Jacquin *et al.* [53]. These results clearly demonstrate the principal effect of system rotation on isotropic turbulence, i.e. increasing rotation rate decreases the decay rate of turbulent kinetic energy. As shown, LES predictions of this phenomenon are in good agreement with the experimental data.

4.4. Turbulent mixing layers

Vreman *et al.* [54] simulated a temporal, weakly compressible (Mach = 0.2) mixing layer in a cubic domain using 192^3 grid resolution. In their study, the length of the domain was $29.5\delta^0_\omega$ (where δ^0_ω denotes the initial vorticity thickness), which corresponds to four times the wavelength of the most unstable mode as predicted by linear stability theory at Mach = 0.2. Periodic boundary conditions are imposed in the streamwise (x) and spanwise (z) directions,

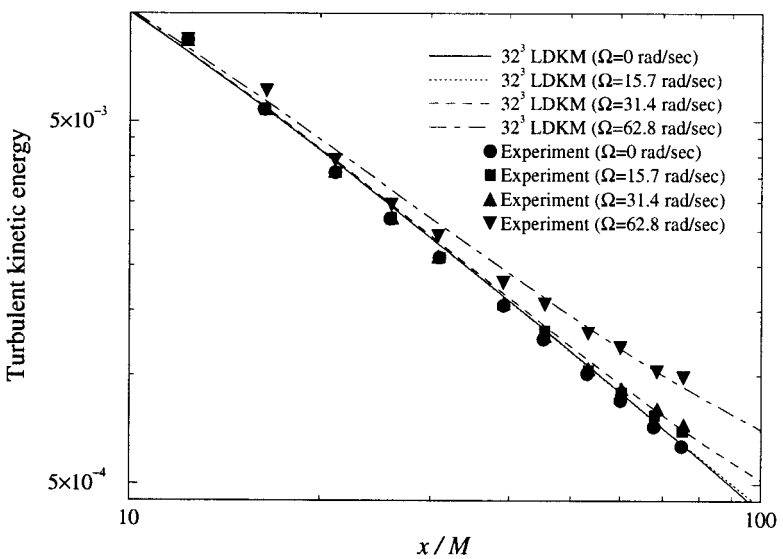

Figure 7. Decay of resolved turbulent kinetic energy predicted by LES of rotating isotropic turbulence for various rotation rates. Experimental data of Jacquin *et al.* [53] are also plotted.

while in the cross-stream (y) direction, the boundaries are assumed as slip walls. The initial velocity field is the hyperbolic–tangent profile, $u = \Delta U \tanh(2y/\delta^0_\omega)$, on which is superimposed a three-dimensional large-amplitude eigenfunction disturbance obtained from linear stability analysis [55]. In the above expression, ΔU is the mean streamwise velocity difference of a mixing layer. Note that, hereafter U, V, W denote respectively the mean streamwise, normal, spanwise velocity components instead of the previously defined contravariant velocities. For the present study, the initial LES field is obtained by filtering the initial DNS field (generated using Vreman's code) for the length of the domain $50\delta^0_\omega$.

Figure 8 shows the time evolution of the momentum thickness δ_m scaled using

$$\delta^*_m(t^*) = \frac{1}{\delta^{\mathrm{S}}_m}[\delta_m(t^*) - \delta^{\mathrm{S}}_m], \tag{45}$$

$$t^* = \frac{\Delta U}{\delta^{\mathrm{S}}_m}(t - t^{\mathrm{S}}), \tag{46}$$

where the superscript * denotes scaled variables and superscript S indicates scaling parameters at the self-similarity starting point. Subtractions by δ^{S}_m and t^{S} are implemented to assign zero scaled time and scaled momentum thickness at the self-similarity starting point. In this study, the self-similarity starting point is estimated by the point where the mixing layer begins to grow linearly. The results of the 192^3 DNS by Vreman *et al.* [56] are also plotted for comparison. As shown, DNS and LES results appear to collapse on each other reasonably well. Figure 8 also includes the asymptotic growth rate (slope) obtained from the experiment of Bell and Mehta [57] for a spatially evolving mixing layer. The growth rates predicted by the LES agree very well with the experiment.

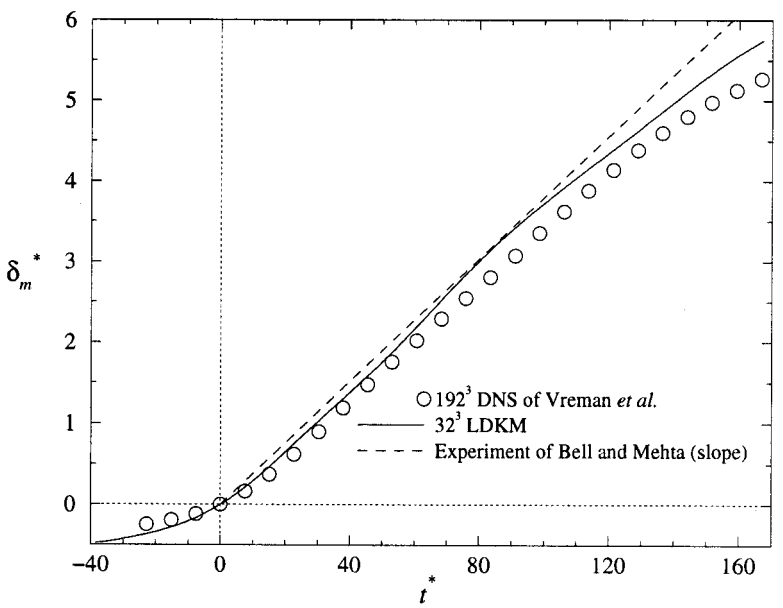

Figure 8. Time variation of the momentum thickness of temporally evolving turbulent mixing layer in scaled co-ordinates using self-similarity starting point parameters. Results of the 192^3 DNS by Vreman *et al.* [56] and experimental data of Bell and Mehta [57] are also plotted.

In Figure 9, mean (ensemble-averaged) velocity profiles U at five time levels (see figure) during the entire period after $t^* = 0$ are plotted with self-similar scaling using the time-dependent momentum thickness δ_m and the velocity difference ΔU. Also included are the experimental data of Bell and Mehta [57]. The collapse of the data at the five time levels is excellent, and the mean profile agrees very well with the data of Bell and Mehta [57].

In Figure 10, Reynolds stress profiles $\widetilde{uv}$ scaled using self-similar parameters at $t^* = 110$ are shown together with the DNS data of Vreman *et al.* [56]. The overall agreement between the DNS and the LES results is quite good. These results confirm the time accuracy of the present solver in the simulation of the coherent structures.

4.5. Turbulent plane Couette flows

The experiments of Bech *et al.* [58] and Aydin and Leutheusser [59,60] were simulated. In the simulations, only the upper wall (at $y/h = 1$, where h is the channel half height) was moving with a constant velocity U_w, while the lower wall (at $y/h = -1$) was fixed. The chosen Reynolds number $Re = U_w h/\nu$ was 2600, while the Reynolds number $Re_\tau = U_\tau h/\nu$ based on the wall shear velocity $U_\tau = (\nu \, \mathrm{d}U/\mathrm{d}y|_{\mathrm{wall}})^{1/2}$ was 81. The computational domain was $4\pi h \times 2h \times 2\pi h$ in the streamwise, normal and spanwise directions, with uniform spacing in the streamwise and spanwise directions, while in the normal direction the grid was stretched using a 6% linear stretching in order to improve the resolution in the near-wall regions. Computational resolution was respectively around $\Delta x^+ = 33.8$ (here $\Delta x^+ = \Delta x U_\tau/\nu$ is the streamwise directional grid width, which is normalized by the viscous scales), $\Delta z^+ = 25.3$ and $\Delta y^+ = 1.6$ (next to the wall) with a maximum of $\Delta y^+ = 9.8$ in the core region. At the walls, no-slip conditions were used and in the homogeneous (streamwise and spanwise) directions, periodic conditions were imposed. The initial field was constructed of the laminar mean velocity profile with finite amplitude velocity fluctuations superimposed. After about $150h/U_w$, the flow reaches a statistically steady state. Statistics were obtained by ensemble averaging for another $55h/U_w$.

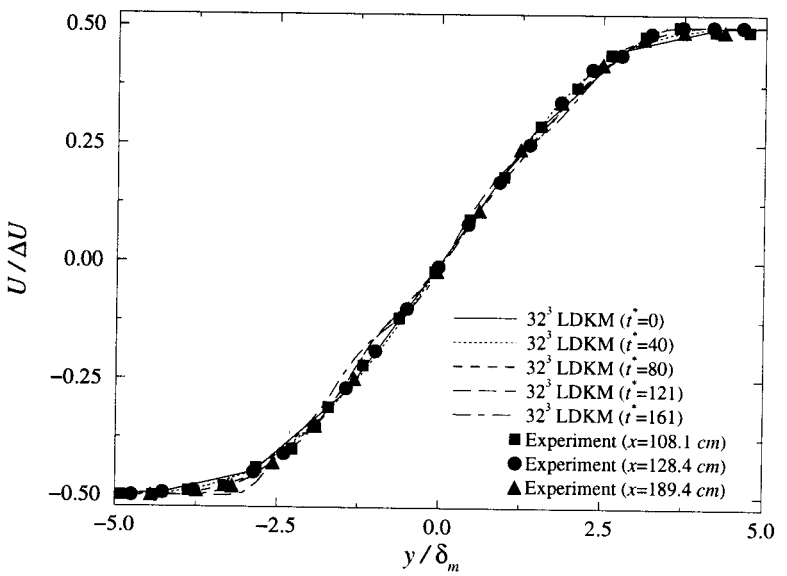

Figure 9. Mean streamwise velocity profiles in self-similar scaled co-ordinates obtained from LES of temporally evolving turbulent mixing layer. Experimental data of Bell and Mehta [57] at three downstream locations are also plotted.

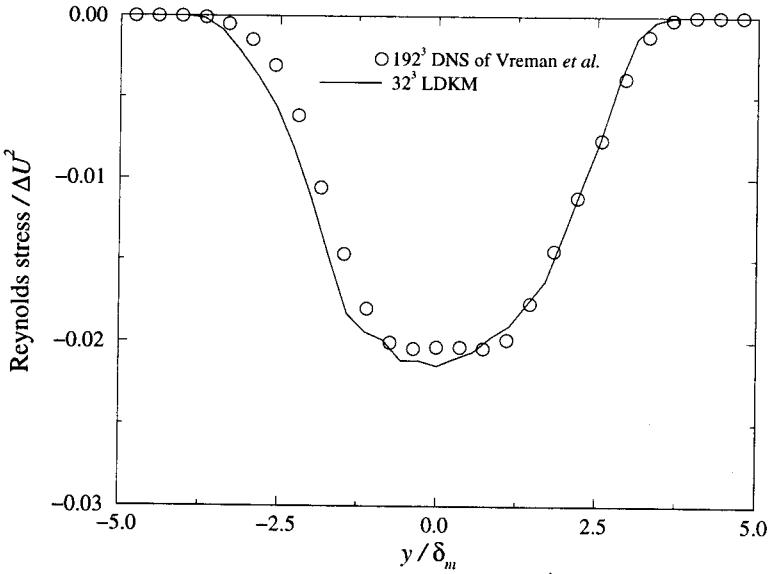

Figure 10. Comparison of time-accurate simulation results obtained from LES of temporally evolving turbulent mixing layer. Reynolds stresses uv at $t^* = 110$ are plotted in self-similar scaled co-ordinates. Results of the 192^3 DNS by Vreman *et al.* [56] are also plotted.

Figure 11(a) and (b) shows the mean velocity distribution. For comparison, experimental data obtained by Aydin and Leutheusser [59] at $Re = 2600$ and Bech *et al.* [58] at $Re = 2520$, and DNS results by Bech *et al.* [58] at $Re = 2600$ are also plotted in Figure 11(a). The DNS [58] was carried out using the $256 \times 70 \times 256$ grid resolution. The agreement between the LES and the experimental data is excellent, both in the wall region and in the center of the channel. In Figure 11(b), the mean velocity is plotted in a semi-logarithm form, normalized by the viscous scales. As shown, the velocity profile is clearly divided into a viscous sublayer, a buffer region and a logarithm part. For comparison, the universal velocity distribution law for smooth-wall conditions is also plotted,

$$U^+ = A \ln y^+ + B, \tag{47}$$

where $U^+ = U/U_\tau$, $y^+ = yU_\tau/\nu$ and A is the inverse of the von Kármán constant. The constants appearing in the equation have the universal values $A = 2.5$ and $B = 5.5$. The LES results align well with the straight line with only small deviations. The logarithmic region extends to the center of the channel, a feature observed in the experiments and also captured here.

In Figure 12, the turbulence intensities (u_{rms}, v_{rms}, w_{rms} are the root-mean-square of fluctuating velocities along the streamwise, normal and spanwise directions respectively) obtained from LES, DNS and experiments are shown (only the moving wall part of the LES results are presented). The LES results show overall good agreement with the DNS and experimental data except for some deviations of the normal component in the region close to the wall. The highest intensity is observed in the streamwise component, which has a maximum at $y^+ \approx 13$, whereas (unlike the plane Poiseuille flow) the other components monotonically increase to a constant value in the center of the channel. In the present simulation, the ratio of the velocity fluctuations $v_{\text{rms}}/u_{\text{rms}} \approx 0.65$ is obtained (this value lies in between the value of 0.6 obtained by Aydin and Leutheusser [60] and the value of 0.67 obtained by Bech *et al.* [58]).

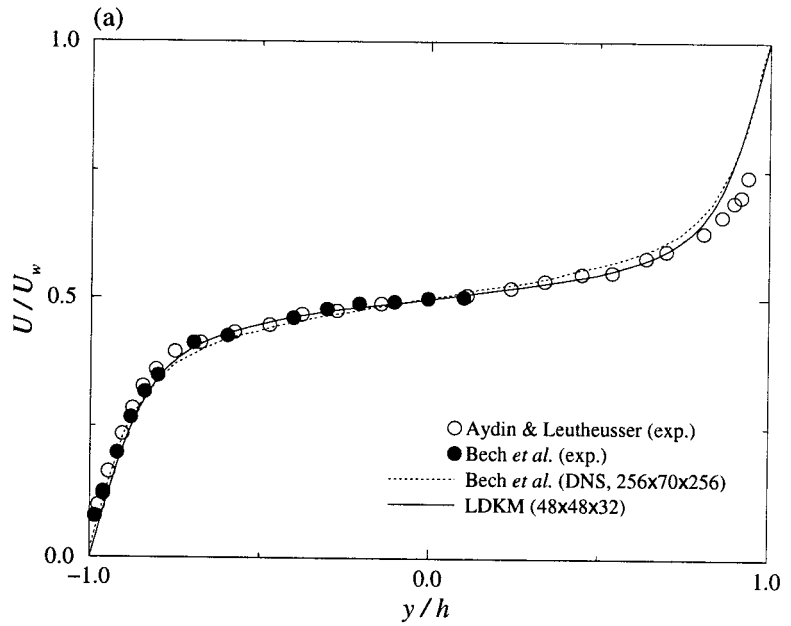

a)

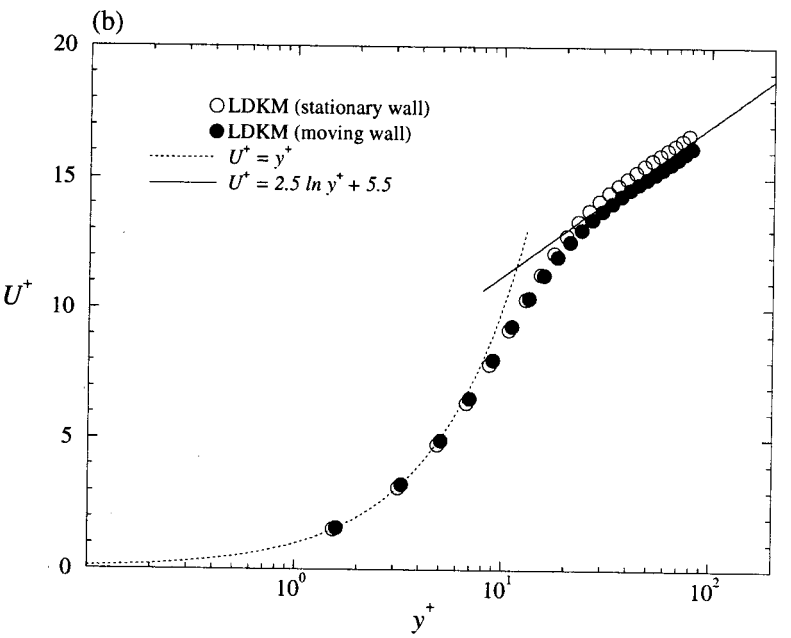

b)

Figure 11. (a) Mean velocity distribution and (b) mean velocity distribution in a semi-logarithm form normalized with viscous scales obtained from turbulent plane Couette flow simulation. Experimental data of Aydin and Leutheusser [59] and Bech *et al.* [58] and DNS results of Bech *et al.* [58] are also plotted in (a). In (b), universal velocity distribution law for smooth wall conditions is plotted for comparison.

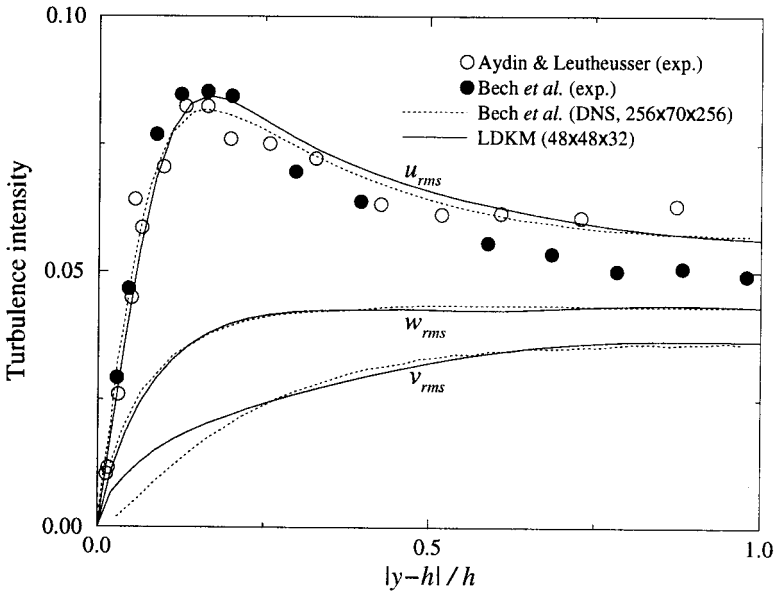

Figure 12. Turbulence intensities obtained from turbulent plane Couette flow simulation. Experimental data of Aydin and Leutheusser [60] and Bech *et al.* [58], and DNS results of Bech *et al.* [58] are also plotted.

In Figure 13, the model coefficient is plotted in a logarithm form to examine the dynamic model behavior in the wall region. Inspection of the LDKM behavior near walls where low-Reynolds number effects are dominant is extremely important because the LDKM is

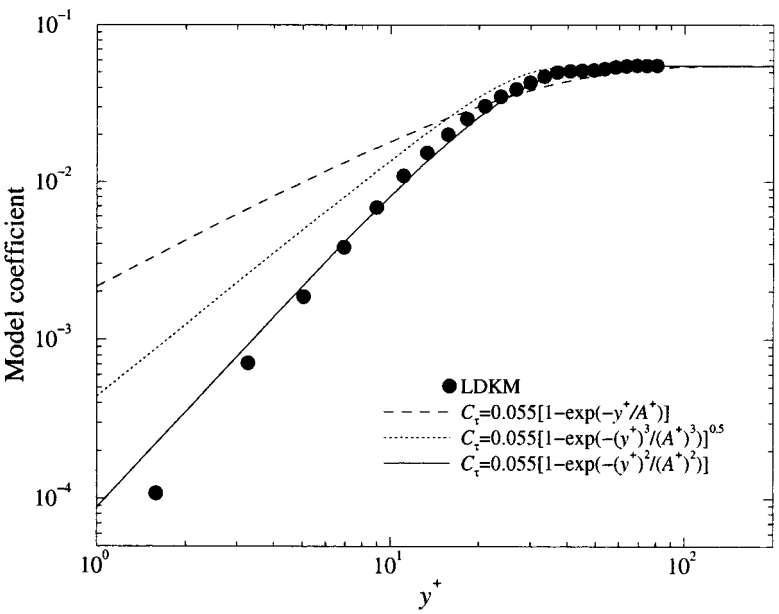

Figure 13. Mean model coefficient distribution in a logarithm form normalized with viscous scales obtained from turbulent plane Couette flow simulation. Some exponential damping functions are also plotted for comparison.

formulated based on experimental observation in high-Reynolds number flows. The result confirms the exponential decay of the dynamically determined model coefficient (and corresponding reduction of the eddy viscosity) in the wall region. The constant model coefficient (here 0.055 is used to match with the present calculation at the core region) distributions are also plotted combined with the exponential damping function as proposed by Moin and Kim [61]

$$C_\tau = 0.055[1 - \exp(-y^+/A^+)], \tag{48}$$

and by Piomelli *et al.* [62]

$$C_\tau = 0.055[1 - \exp(-(y^+)^3/(A^+)^3)]^{1/2}, \tag{49}$$

with wall damping constant $A^+ = 25$. These damping functions were determined from *a priori* tests (where the exact SGS quantities are calculated from exact DNS data and then the modeled quantities are evaluated by comparison with the exact ones) developed by Clark *et al.* [63]. In most cases, however, the *a priori* test results differ from those of *a posteriori* tests since, in *a priori* tests, the results are obtained by completely ignoring the dynamics at the cut-off. The present results best match with the following damping function, which is little different from the above damping functions based on *a priori* tests:

$$C_\tau = 0.055[1 - \exp(-(y^+)^2/(A^+)^2)]. \tag{50}$$

4.6. Turbulent recirculating flows

The experiment of lid-driven, three-dimensional cavity flows of Prasad and Koseff [64] is simulated. In the experiment, the three-dimensional cavity has a square cross-section (i.e. width

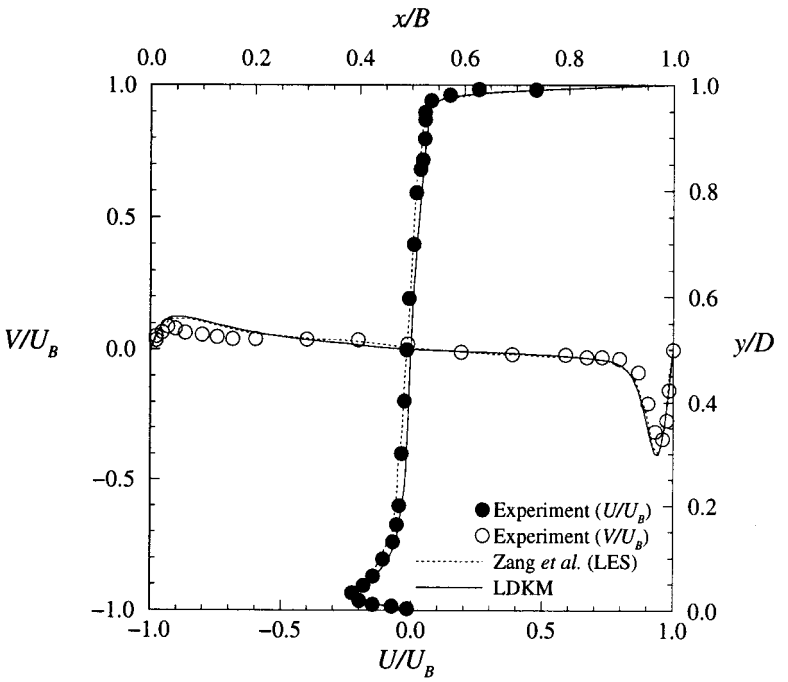

Figure 14. Mean velocity distributions on the centerlines in the midplane obtained from turbulent recirculating flow simulation. LES results of Zang *et al.* [44] and experimental data of Prasad and Koseff [64] are also plotted.

(B) = depth (D)) and spanwise aspect ratio (SAR = L/B, where L is the cavity span) of 0.5:1. The lid (the top wall) is moving at a velocity U_B and the other walls (i.e. the upstream and downstream walls, which are perpendicular to the streamwise (x) direction, the bottom wall which is perpendicular to the vertical (y) direction, and the side walls, which are perpendicular to the spanwise (z) direction), remain stationary. Hence, fluid motions are developed by the shear of the lid, resulting in a complicated three-dimensional flow field consisting of a stationary primary vortex and a number of complex secondary corner vortices. In these flows, the Reynolds number is usually defined to be $Re = U_B B/\nu$. Koseff and Street [65] have shown that at Reynolds number higher than about 6000, instability occurs near the downstream corner vortex. As the Reynolds number increases, the flow becomes increasingly turbulent near walls, and at Reynolds numbers higher than 10000, the flow near the downstream corner vortex becomes fully turbulent. In the present study, the Reynolds number of 10000 is considered.

The simulation was carried out using a $64 \times 64 \times 32$ grid, which is stretched in the streamwise and vertical directions using 6.5% and 13.4% linear stretching respectively, but is uniform in the spanwise direction. Small random velocity perturbations are initially prescribed to prevent the initial k_{SGS} field from becoming zero. The computation was first conducted with a 32^3 grid. After the flow was fully developed, the coarser resolution field was interpolated onto the finer resolution field. Simulation was then continued and statistics were collected after a sufficient relaxation time.

The three-dimensional flow in a cubic cavity has a very complex structure. The main structure of the flow is similar to that in a two-dimensional square cavity but is significantly

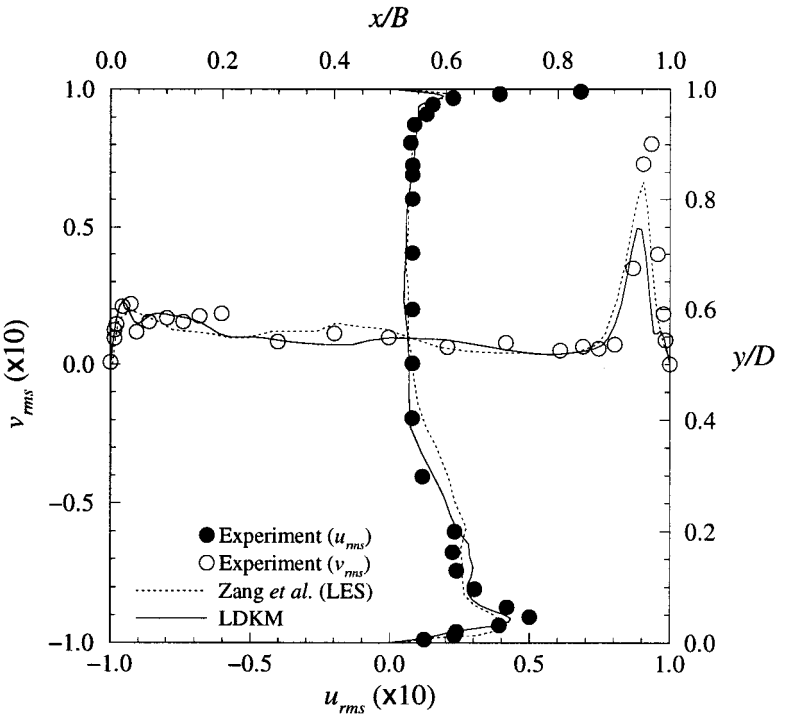

Figure 15. Turbulence intensities on the centerlines in the midplane obtained from turbulent recirculating flow simulation. LES results of Zang *et al.* [44] and experimental data of Prasad and Koseff [64] are also plotted.

more complicated due to the side walls. In planes perpendicular to the z-direction, the flow field consists of a primary vortex with two corner vortices at the bottom wall and a vortex at the top upstream corner. The strengths of these vortices vary with the distance from the side walls. In the midplane, the strengths of the vortices are strongest due to the viscous damping at the side walls. In planes perpendicular to the x-direction, the flow field also consists of vortices. The complete details of the observed three-dimensional flow field are not presented here for brevity.

Figure 14 shows the computed mean streamwise (U) and vertical (V) velocity profiles on the centerlines in the midplane. Measurements by Prasad and Koseff [64] are given for comparison. LES results by Zang *et al.* [44], which were obtained using the dynamic mixed model (DMM) on the same grid resolution ($64 \times 64 \times 32$), are also shown. The DMM was formulated by employing the mixed model (where the Smagorinsky-type eddy viscosity model is combined with the scale similarity model to parameterize the SGS stress) as a base model and, therefore, does not require alignment of the SGS stress tensor and the strain rate tensor. In this dynamic procedure, the model coefficient was also calculated locally by test filtering the model coefficient field. Zang *et al.* [44] have demonstrated the superiority of the DMM over the conventional dynamic Smagorinsky model of Germano *et al.* [8] by showing a better agreement of fluctuating velocity statistics with experiments in the simulation of the recirculating flows at $Re = 7500$. As shown in the figure, the predicted profiles by the LDKM and the DMM LES are very close to each other and agree well with the experimental data except that both calculations overpredict the maximum vertical velocity and the thickness of the boundary layers on the upstream wall ($x/B = 0$).

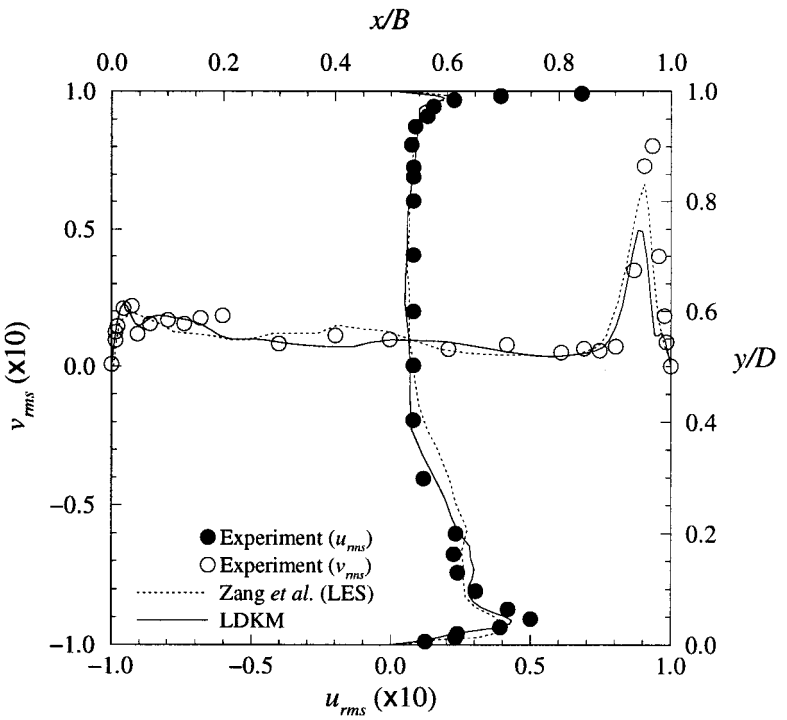

Figure 16. Reynolds stress profiles on the centerlines in the midplane obtained from turbulent recirculating flow simulation. LES results of Zang *et al.* [44] and experimental data of Prasad and Koseff [64] are also plotted.

The turbulence intensities (u_{rms} along the streamwise direction and v_{rms} along the normal direction) on the centerlines in the midplane are shown in Figure 15. Note that this is multiplied by a factor of 10 for a better presentation. Both calculations show a good overall agreement with the experiment although they both underpredict the magnitude of the peaks. Note that the LDKM computation captures the two humps in the experimental profile on the upstream wall (at $x/B \approx 0$) with reasonable accuracy, while the DMM prediction shows only one hump.

Figure 16 displays the centerline Reynolds stress profiles on the midplane. This quantity is magnified by a factor of 500 for a presentation purpose. Both LESs predict the profiles fairly accurately. The LDKM gives a better agreement with the experiment than the DMM in the profiles along the bottom half of the vertical centerline and near the downstream wall ($x/B = 1$), but it overpredicts the experimental data near the upstream wall.

As was experimentally observed [65] for laminar flows, Taylor–Goertler-like (TGL) vortices are present in the downstream secondary eddy region. These vortices are mainly responsible for momentum transfer in laminar flows. On the other hand, for turbulent flows, high-frequency fluctuations play a dominant role in momentum transfer. These fluctuations also destroy the coherence of the TGL vortices. The side walls and the corresponding SAR significantly affect the cavity flows. The side walls reduce the high-frequency fluctuations by increasing viscous damping. As the SAR reduces, these fluctuations are further suppressed. Finally, for high-Reynolds number flows at low SAR, such as the present case, coherent structures reappear in the form of single vortices. The existence of the single vortices is

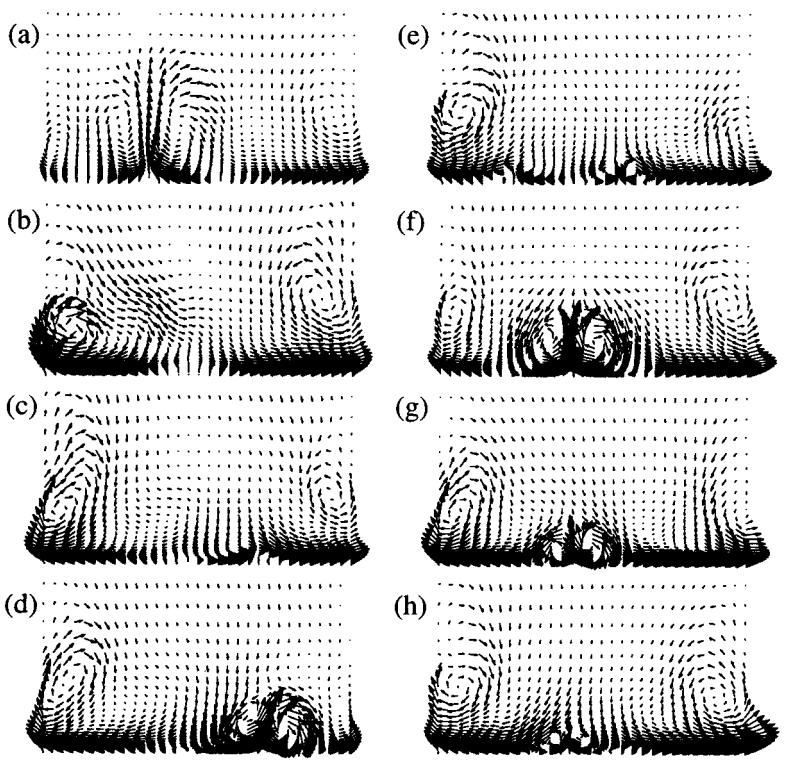

Figure 17. Instantaneous velocity vectors in the y–z plane $0.25B$ from the downstream wall of turbulent recirculating flow. Eight different instantaneous results are shown in time sequence with uniform time interval of 4 $U_B t/B$.

confirmed in Figure 17, which shows instantaneous velocity vectors in the $y-z$ plane (only $\frac{1}{4}$ of the plane from the bottom wall is presented) at $0.25B$ from the downstream wall. Eight different instantaneous results are shown in time sequence with uniform time interval of $4\ U_B t/B$. One can see that the single vortices repeatedly generated and destroyed while they are interacting with the side walls.

5. CONCLUSIONS

In this paper, a numerical method based on the well-known pseudo-compressibility approach has been studied to determine its capability to accurately and efficiently solve the unsteady incompressible Navier–Stokes equations for turbulent flows. The ability of this scheme to carry out LES is demonstrated in this paper by incorporating a localized dynamic subgrid model based on the transport equation for the subgrid kinetic energy. Time accurate results were obtained by using a dual time stepping technique, which is based on the artificial compressibility method. Adequate spatial accuracy was achieved by employing high-order-accurate finite differences. Finally, the fully implicit primitive variable formulation is efficiently solved by adopting various convergence–acceleration techniques, which reduce significantly the number of subiterations. Results established the accuracy and the efficiency of the present solver for unsteady turbulent flow simulations.

ACKNOWLEDGMENTS

The authors wish to thank Professor B. Vreman for providing the initial disturbance field generator of turbulent mixing layer and the data presented in Figures 8 and 10. This work was supported by the Fluid Dynamics Division of the Office of Naval Research under Grant N00014-93-1-0342. monitored by Dr L.P. Purtell. Computing time was provided by the DoD High Performance Computing (HPC) Centers: Army Research Laboratory (ARL), Naval Oceanographic Office (NAVOCEANO), and Army Engineer Waterways Experiment Station (CEWES).

REFERENCES

1. S.E. Rogers and D. Kwak, 'Upwind differencing scheme for the time-accurate incompressible Navier–Stokes equations', *AIAA J.*, **28**, 253–262 (1990).
2. W.-G. Park, 'A three-dimensional multigrid technique for unsteady incompressible viscous flows', *Ph.D. Thesis*, Georgia Institute of Technology, Atlanta, GA, 1993.
3. Y. Zang, R.L. Street and J.R. Koseff, 'A non-staggered grid, fractional step method for time-dependent incompressible Navier–Stokes equations in curvilinear coordinates', *J. Comput. Phys.*, **114**, 18–33 (1994).
4. M.M. Rail and P. Moin, 'Direct simulations of turbulent flow using finite difference schemes', *J. Comput. Phys.*, **96**, 15–53 (1991).
5. S.K. Lele, 'Compact finite difference schemes with spectral-like resolution', *J. Comput. Phys.*, **103**, 16–42 (1992).
6. H. Choi and P. Moin, 'Effects of the computational time step on numerical solutions of turbulent flows', *J. Comput. Phys.*, **113**, 1–4 (1994).
7. J. Smagorinsky, 'General circulation experiments with the primitive equations', *Mon. Weather Rev.*, **91**, 99–164 (1963).
8. M. Germano, U. Piomelli, P. Moin and W.H. Cabot, 'A dynamic subgrid-scale eddy viscosity model', *Phys. Fluids A*, **3**, 1760–1765 (1991).
9. W.H. Cabot and P. Moin, 'Large eddy simulation of scalar transport with the dynamic subgrid-scale model', in B. Galperin and S. Orszag (eds.), *LES of Complex Engineering and Geophysical Flow*, Cambridge University Press, Cambridge, 1993, pp. 141–158.
10. T.S. Lund, S. Ghosal and P. Moin, 'Numerical experiments with highly-variable eddy viscosity models', in U. Piomelli and S. Ragab (eds.), *Engineering Applications of Large Eddy Simulations*, vol. 162 of FED, ASME, New York, 1993, pp. 7–11.

11. W.-W. Kim and S. Menon, 'A new dynamic one-equation subgrid-scale model for large eddy simulations', *AIAA-95-0356*, 1995.
12. D. Kwak, 'Computation of viscous incompressible flows', Technical Report, *NASA Technical Memorandum 101090*, National Aeronautics and Space Administration, 1989.
13. M. Breuer and D. Hänel, 'A dual time-stepping method for 3D, viscous, incompressible vortex flows', *Comput. Fluids*, **22**, 467–484 (1993).
14. S. Menon, P.-K. Yeung and W.-W. Kim, 'Effect of subgrid models on the computed interscale energy transfer in isotropic turbulence', *Comput. Fluids*, **25**, 165–180 (1996).
15. R.S. Rogallo, 'Numerical experiments in homogeneous turbulence', Technical Report, *NASA Technical Memorandum 81315*, National Aeronautics and Space Administration, 1981.
16. W.-W. Kim, 'A new dynamic subgrid-scale model for large eddy simulation of turbulent flows', *Ph.D. Thesis*, Georgia Institute of Technology, Atlanta, GA, September 1996.
17. U. Schumann, 'Subgrid scale model for finite difference simulations of turbulent flows in plane channels and annuli', *J. Comput. Phys.*, **18**, 376–404 (1975).
18. S. Menon and W.-W. Kim, 'High Reynolds number flow simulations using the localized dynamic subgrid-scale model', *AIAA-96-0425*, 1996.
19. S. Liu, C. Meneveau and J. Katz, 'On the properties of similarity subgrid-scale models as deduced from measurements in a turbulent jet', *J. Fluid Mech.*, **275**, 83–119 (1994).
20. A. Yoshizawa and K. Horiuti, 'A statistically-derived subgrid-scale kinetic energy model for the large eddy simulation of turbulent flows', *J. Phys. Soc. Jpn.*, **54**, 2834–2839 (1985).
21. E.T. Spyropoulos and G.A. Blaisdell, 'Evaluation of the dynamic subgrid-scale model for large eddy simulations of compressible turbulent flows', *AIAA-95-0355*, 1995.
22. F.M. Najjar and D.K. Tafti, 'Study of discrete test filters and finite difference approximations for the dynamic subgrid-scale stress model', *Phys. Fluids*, **4**, 1076–1088 (1996).
23. J. Bardina, J.H. Ferziger and W.C. Reynolds, 'Improved subgrid scale models for large eddy simulation', *AIAA-80-1357*, 1980.
24. D.K. Lilly, 'A proposed modification of the Germano subgrid-scale closure method', *Phys. Fluids A*, **4**, 633–635 (1992).
25. P. Moin, K. Squires, W. Cabot and S. Lee, 'A dynamic subgrid-scale model for compressible turbulence and scalar transport', *Phys. Fluids A*, **11**, 2746–2754 (1991).
26. V.C. Wong, 'A proposed statistical-dynamic closure method for the linear or nonlinear subgrid-scale stresses', *Phys. Fluids A*, **4**, 1080–1082 (1992).
27. C. Fureby, G. Tabor, H.G. Weller and A.D. Gosman, 'A comparative study of subgrid scale models in homogeneous isotropic turbulence', *Phys. Fluids*, **9**, 1416–1429 (1997).
28. U. Schumann, 'Realizability of Reynolds-stress turbulence models', *Phys. Fluids*, **20**, 721–725 (1976).
29. D.A. Anderson, J.C. Tannehill and R.H. Pletcher, *Computational Fluid Mechanics and Heat Transfer*, McGraw-Hill, New York, 1984.
30. D. Carati, S. Ghosal and P. Moin, 'On the representation of backscatter in dynamic localization models', *Phys. Fluids*, **7**, 606–616 (1995).
31. F.H. Harlow and J.E. Welch, 'Numerical calculation of time-dependent viscous incompressible flow with free surfaces', *Phys. Fluids*, **8**, 2182–2189 (1965).
32. C.M. Rhie and W.L. Chow, 'Numerical study of the turbulent flow past an airfoil with trailing edge separation', *AIEE J.*, **21**, 1525–1532 (1983).
33. S.W. Armfield, 'Finite difference solution of the Navier–Stokes equations on staggered and non-staggered grids', *Comput. Fluids*, **20**, 1–17 (1991).
34. J.C. Strikwerda, 'Finite difference methods for the Stokes and Navier–Stokes equations', *SIAM J. Sci. Statist. Comput.*, **5**, 56–68 (1984).
35. A.J. Chorin, 'Numerical solution of Navier–Stokes equations', *Math. Comput.*, **22**, 745–762 (1968).
36. A.J. Chorin, 'A numerical method for solving incompressible viscous flow problems', *J. Comput. Phys.*, **2**, 12–26 (1967).
37. E. Turkel, 'Preconditioned methods for solving the incompressible and low speed compressible equations', *J. Comput. Phys.*, **72**, 277–298 (1987).
38. P.R. McHugh and J.D. Ramshaw, 'Damped artificial compressibility iteration scheme for implicit calculations of unsteady incompressible flow', *Int. J. Numer. Methods Fluids*, **21**, 141–153 (1995).
39. Y.P. Marx, 'Time integration schemes for the unsteady incompressible Navier–Stokes equations', *J. Comput. Phys.*, **112**, 182–209 (1994).
40. R.W. MacCormack, 'An efficient numerical method for solving the time-dependent compressible Navier–Stokes equations at high Reynolds number', Technical Report, *NASA Technical Memorandum x-73*, National Aeronautics and Space Administration, 1976.
41. A. Jameson, 'Solution of the Euler equations for two-dimensional transonic flow by a multigrid method', *Appl. Math. Comput.*, **13**, 327–355 (1983).
42. A. Brandt, *Guide to Multigrid Development*, *Vol. 960 of Lecture Notes in Mathematics*, Springer, Berlin, 1981, pp. 220–312.
43. S. Saini and D.H. Bailey, 'NAS parallel benchmark (Version 1.0). Results 11-96', Technical Report, *Report NAS-96-18*, Numerical Aerospace Simulation Program, NASA, Ames Research Center, 1996.

44. Y. Zang, R.L. Street and J.R. Koseff, 'A dynamic mixed subgrid-scale model and its application to turbulent recirculating flows', *Phys. Fluids A*, **5**, 3186–3196 (1993).
45. J.S. Baggett, J. Jimenez and A.G. Kravchenko, 'Resolution requirements in large eddy simulations of shear flows', Center For Turbulent Research, Annual Research Briefs, 1997, pp. 51–66.
46. J.H. Ferziger, 'Recent advances in large eddy simulation', in W. Rodi and G. Bergeles (eds.), *Engineering Turbulence Modeling and Experiments 3*, Elsevier Science, Amsterdam, 1996, pp. 163–175.
47. G. Comte-Bellot and S. Corsin, 'Simple Eulerian time correlation of full- and narrow-band velocity signals in grid-generated, ''isotropic'' turbulence', *J. Fluid Mech.*, **48**, 273–337 (1971).
48. S. Ghosal, T.S. Lund, P. Moin and K. Akselvoll, 'A dynamic localization model for large eddy simulation of turbulent flows', *J. Fluid Mech.*, **286**, 229–255 (1995).
49. A. Vincent and M. Meneguzzi, 'The spatial structure and statistical properties of homogeneous turbulence', *J. Fluid Mech.*, **225**, 1–20 (1991).
50. J. Jimenez, A.A. Wray, P.S. Saffman and R.S. Rogallo, 'The structure of intense vorticity in isotropic turbulence', *J. Fluid Mech.*, **255**, 65–90 (1993).
51. R.M. Kerr, 'Higher order derivative correlations and the alignment of small-scale structures in isotropic numerical turbulence', *J. Fluid Mech.*, **153**, 31–58 (1985).
52. M. Briscolini and P. Santangelo, 'The non-Gaussian statistics of the velocity field in low-resolution large eddy simulations of homogeneous turbulence', *J. Fluid Mech.*, **270**, 199–217 (1994).
53. L. Jacquin, O. Leuchter, C. Cambon and J. Mathieu, 'Homogeneous turbulence in the presence of rotation', *J. Fluid Mech.*, **220**, 1–52 (1990).
54. B. Vreman, B. Geurts and H. Kuerten, 'Comparison of numerical schemes in large eddy simulation of the temporal mixing layer', *Int. J. Numer. Methods Fluids*, **22**, 297–311 (1996).
55. N.D. Sandham and W.C. Reynolds, 'Three-dimensional simulations of large eddies in the compressible mixing layer', *J. Fluid Mech.*, **224**, 133–158 (1991).
56. B. Vreman, B. Geurts and H. Kuerten, 'On the formulation of the dynamic mixed subgrid-scale model', *Phys. Fluids*, **6**, 4057–4059 (1994).
57. J.H. Bell and R.D. Metha, 'Development of a two-stream mixing layer from tripped and untripped boundary layers', *AIAA J.*, **28**, 2034–2042 (1990).
58. K.H. Bech, N. Tillmark, P.H. Alfredsson and H.I. Andersson, 'An investigation of turbulent plane Couette flow at low Reynolds numbers', *J. Fluid Mech.*, **286**, 291–325 (1995).
59. E.M. Aydin and H.J. Leutheusser, 'Experimental investigation of turbulent plane Couette flow', in W.W. Bower (ed.), *Forum on Turbulent Flows*, Vol. 51 of FED, ASME, New York, 1987, pp. 51–54.
60. E.M. Aydin and H.J. Leutheusser, 'Plane-Couette flow between smooth and rough walls', *Exp. Fluids*, **11**, 302–312 (1991).
61. P. Moin and J. Kim, 'Numerical investigation of turbulent channel flow', *J. Fluid Mech.*, **118**, 341–377 (1982).
62. U. Pionlelli, J.H. Ferziger and P. Moin, 'Models for large eddy simulations of turbulent channel flows including transpiration', Technical Report, *Report TF-32*, Department of Mechanical Engineering Stanford University, 1987.
63. R.A. Clark, J.H. Ferziger and W.C. Reynolds, 'Evaluation of subgrid-scale models using an accurately simulated turbulent flow', *J. Fluid Mech.*, **91**, 1–16 (1979).
64. A.K. Prasad and J.R. Koseff, 'Reynolds number and end-wall effects on a lid-driven cavity flow', *Phys. Fluids A*, **1**, 208–218 (1989).
65. J.R. Koseff and R.L. Street, 'Visualization studies of a shear driven three-dimensional recirculating flow', *J. Fluids Eng.*, **106**, 21–29 (1984).

